Parameterization of Submesoscale Mixed Layer Restratification under Sea Ice

KALYAN SHRESTHA[a] AND GEORGY E. MANUCHARYAN[a]

[a] *School of Oceanography, University of Washington, Seattle, Washington*

(Manuscript received 2 February 2021, in final form 7 December 2021)

ABSTRACT: Commonly used parameterization of mixed layer instabilities in general circulation models was developed for temperate oceans and does not take into account the presence of sea ice in any way. However, the ice–ocean drag provides a strong mechanical coupling between the sea ice and the surface ocean currents and hence may affect mixed layer restratification processes. Here we use idealized simulations of mixed layer instabilities to demonstrate that the sea ice dramatically suppresses the eddy-driven overturning in the mixed layer by dissipating the eddy kinetic energy generated during instabilities. Considering the commonly used viscous-plastic sea ice rheology, we developed an improvement to the existing mixed layer overturning parameterization, making it explicitly dependent on sea ice concentration. Below the critical sea ice concentration of about 0.68, the internal sea ice stresses are very weak and the conventional parameterization holds. At higher concentrations, the sea ice cover starts acting as a nearly immobile surface lid, inducing strong dissipation of submesoscale eddies and reducing the intensity of the restratification streamfunction up to a factor of 4 for a fully ice-covered ocean. Our findings suggest that climate projection models might be exaggerating the restratification processes under sea ice, which could contribute to biases in mixed layer depth, salinity, ice–ocean heat fluxes, and sea ice cover.

KEYWORDS: Sea ice; Ageostrophic circulations; Eddies; Streamfunction; Mixed layer; Parameterization

1. Introduction

Oceanic surface mixed layer mediates the exchange of heat, mass, momentum, and other tracers across the ocean and thus plays an important role in global climate (Melville 1996; Csanady 2001; Sallée et al. 2012; Abernathey et al. 2016). Mixed layers host a large variety of physical processes, ranging from small-scale vertical processes with $O(<100)$ m length scales (e.g., Langmuir cells; Langmuir 1938; McWilliams et al. 1997; Shrestha et al. 2018) to large-scale horizontal motions characterized by mesoscale eddies with scales of $O(10–100)$ km (Ferrari and Wunsch 2009). There are also processes with an intermediate range of horizontal scales $O(0.1–10)$ km and time scales $O(1)$ day (Boccaletti et al. 2007; Fox-Kemper et al. 2008) that dominate the budgets of heat, momentum, and salt in surface mixed layers. These are submesoscale processes that are characterized by $O(1)$ Richardson number and Rossby number dynamics and intense localized vertical velocities of $O(10–100)$ m day^{-1}, which emphasize their key role in the vertical tracer transport. Submesoscale processes are known to increase vertical velocities and tracer transport by 5 times compared to large-scale mesoscale processes (Bachman et al. 2017; Klein and Lapeyre 2009; Su et al. 2018). Submesoscale eddies in the surface mixed layer can be generated due to various mechanisms such as mixed layer instabilities (MLI) (Boccaletti et al. 2007), vertical shear instabilities, mesoscale frontogenesis (Spall 1997), or topographical wakes (Molemaker et al. 2015). It is known that these submesoscale eddies, driven by wind forces and/or lateral buoyancy gradients, hugely affect nutrient and heat fluxes in the upper ocean (Thomas and Ferrari 2008; Callies et al. 2015; McWilliams 2016; Thompson et al. 2016). Eddies can also interact with wind-driven flows that enhance or reduce their strength depending on the direction of the wind relative to the front (Thomas and Lee 2005; Mahadevan et al. 2012; du Plessis et al. 2019).

Lateral density fronts in a weakly stratified surface mixed layer undergo restratification by slumping the near-vertical isopycnals that initiate with a gravitational overturning but are subsequently modified by the Rossby adjustment process (Ou 1984; Tandon and Garrett 1995). These Rossby-adjusted fronts further undergo restratification due to agesotrophic baroclinic instabilities and ensue the most dynamical restratification process (Boccaletti et al. 2007) relative to previous mechanisms. Restratification is associated with a release of potential energy stored in the lateral density fronts. More detailed discussions on the characteristics of these instabilities can be found in Stone's (1970) linear instability analysis of the Eady's (1949) problem, where the theory predicts the growth rates and length and time scales of the fastest-growing nongeostrophic modes.

Following Gent and McWilliams's (1990) parameterization for mesoscale restratification, Fox-Kemper and Ferrari (2008) and Fox-Kemper et al. (2008, 2011) proposed a parameterization of mixed layer eddy (MLE) restratification. The parameterization defines an eddy-driven overturning streamfunction, with its strength determined through scaling arguments and its vertical structure based on empirical functions. The overturning streamfunction predicts the submesoscale eddy buoyancy fluxes in relation to the restratification, and its magnitude is a function of lateral buoyancy gradients and mixed layer depth. Such parameterization is a crucial part of global ocean simulations and has been incorporated in many, if not all, climate projection models.

Supplemental information related to this paper is available at the Journals Online website: https://doi.org/10.1175/JPO-D-21-0024.s1.

Corresponding author: Kalyan Shrestha, kalyansh@uw.edu

DOI: 10.1175/JPO-D-21-0024.1

The focus of our study is on mixed layer instabilities in ice-covered regions. Capturing accurate trends of global sea ice extent with climate projection models is a challenging problem (Stroeve et al. 2012; Notz and Community 2020; Roach et al. 2020; Davy and Outten 2020), with marginal ice zones (MIZs) being regions of major prediction uncertainties (Tietsche et al. 2014). MIZs are regions that separate ice pack from the open ocean and commonly accommodate strong lateral buoyancy, salinity, and temperature gradients in the mixed layer (Buckley et al. 1979; Lu et al. 2015; Gallaher et al. 2016). Submesoscale eddies forming as a result of mechanical and thermodynamical interactions with the sea ice can affect the MIZs dynamics (Manucharyan and Thompson 2017; Timmermans et al. 2012; Biddle and Swart 2020; Brenner et al. 2020). Eddy interactions with sea ice can result in an Ekman-pumping-driven vertical transport of subsurface warm waters toward surface sea ice cover (Gupta et al. 2020). Submesoscale eddies are also capable of stirring the surface ocean temperatures and affecting the ice–ocean heat fluxes by bringing warm waters in contact with surface sea ice (Perovich 2003). While submesoscale ocean variability can be generated at meltwater fronts (resulting from melt/growth of sea ice) due to spatially heterogenous salinity and buoyancy fluxes (Manucharyan and Thompson 2017; Lu et al. 2015), the presence of sea ice cover could also dampen under-ice mixed layer eddies (Mensa and Timmermans 2017; Timmermans et al. 2012). The lateral heat transport and mixing induced by the baroclinic eddies generated at ice floe edges could affect the overall sea ice melting Horvat and Tziperman (2018), although this effect is expected to be relevant under low-wind conditions. Biddle and Swart (2020) suggest improvements on existing parameterizations for estimating submesoscale fluxes, which involves replacing the wind stress with ice–ocean stress in the Ekman buoyancy flux calculation to understand the influence of sea ice cover on the wind–front interactions at the submesoscale. This resulted in a 50% reduction in the Ekman buoyancy flux, indicating dampening of submesoscale eddies due to sea ice. However, it was noted that the estimation of Ekman buoyancy flux is prone to error due to the uncertainty in ice–ocean stress parameterization (Smith et al. 2019). However, despite the complexities of ice–ocean interactions, the commonly used parameterization of MLE dynamics (Fox-Kemper et al. 2008) does not account for the presence of sea ice, but it is used in ice-covered polar oceans.

In this paper, we construct a set of idealized simulations of mixed layer instabilities to investigate the impact of mechanical ice–ocean interactions on the submesoscale eddy-induced overturning streamfunction in the mixed layer. Specifically, we explore the impact of the quadratic ice–ocean stress on mixed layer instabilities. Following Fox-Kemper et al. (2008), we consider the spindown of preexisting fronts that may have been generated via mesoscale frontogenesis or heterogeneous buoyancy forcing associated with the sea ice growth/melt or due to the discontinuous nature of sea ice (Cohanim et al. 2021). We note that the mixed layer dynamics can also be impacted by surface wind and temperature forcing (Swart et al. 2020; Giddy et al. 2021) or brine rejection process (Biddle and Swart 2020), or under-ice roughness conditions (Gallaher 2019). However, these complications are out of the scope of this study. Here we focus on generalizing the mixed layer parameterization proposed by Fox-Kemper et al. (2008) to ice-covered regions.

The paper is organized as follows. Section 2 describes the idealized numerical experiments of under-ice frontal spindown. Section 3 demonstrates the characteristics of submesoscale eddies in the mixed layer simulations. Section 4 compares eddy kinetic energy budget terms for the "no sea ice cover" and "full sea ice cover" reference cases. Section 5 includes a derivation establishing a relation between sea ice concentration and associated frictional dissipation through scaling arguments. Section 6 provides a comprehensive discussion on an updated parameterization scheme that depends on sea ice concentration. Section 7 outlines the sensitivity to the sea ice rheology parameters. Finally, section 8 provides a summary of the proposed parameterization and our conclusions.

2. Methodology

a. Numerical model configuration

The MIT general circulation model (Marshall et al. 1997) solves the equations of motion of sea ice (Losch et al. 2010) as

$$m\frac{D\mathbf{u}_I}{Dt} = -mf\mathbf{k}\times\mathbf{u}_I + \boldsymbol{\tau}_{I-O} - m\nabla\phi(0) + \nabla\cdot\boldsymbol{\sigma} \tag{1}$$

$$\frac{\partial m}{\partial t} = -\nabla\cdot(\mathbf{u}_I m), \tag{2}$$

where m is the sea ice mass per unit area that is defined as ch (c represents sea ice concentration, and h represents the mean thickness that remains constant throughout the simulation), $\mathbf{u} = ui + vj$ is the horizontal velocity vector, $\boldsymbol{\sigma}$ is the internal sea ice stress tensor, and I stands for the ice variables. Although the equation shows a material derivative of ice velocity, the nonlinear advection of sea ice momentum is neglected in the MITGCM. Further, in Eq. (1), f is the Coriolis parameter, and $\nabla\phi(0)$ is the gradient of the sea surface height potential that is created due to ocean dynamics below ($g\eta$) and sea ice loading from above (mg/ρ_0), such that $\phi(0) = g\eta + mg/\rho_0$ where g denotes gravity acceleration, and ρ_0 is the reference density. The $\boldsymbol{\tau}$ represents stresses, where index I–O indicate stresses due to ocean–ice interactions. In our simulations, the effect of the atmospheric loading is omitted, which is reflected in the above sea ice momentum equation. The ice–ocean stress that drives sea ice motions in our simulations is parameterized as a quadratic drag law:

$$\boldsymbol{\tau}_{I-O} = \rho_0 c C_d(\mathbf{u}_O - \mathbf{u}_I)|\mathbf{u}_O - \mathbf{u}_I|, \tag{3}$$

where a constant value for drag coefficient is adopted in our simulations, $C_d = 5.35\times10^{-3}$, and $\mathbf{u}_O$ represents near surface ocean current.

The MITgcm sea ice model employs viscous-plastic (VP) rheology (Hibler 1979) that represents the ice floe interactions using nonlinear viscous-plastic compressible fluid in a continuous media. The VP rheology enters the ice momentum

equation as the divergence of the internal stress tensor that depends on the ice strain rate and strength through prescribed constitutive laws (Hibler 1979; Zhang and Hibler 1997). The ice strength is taken to be a function of thickness and concentration, which is expressed as follows:

$$P = P^* m \exp\left[-C^*(1 - c)\right], \tag{4}$$

where P is ice pressure and P^*, C^* are empirical constants. VP model is designed based on the idea that the collection of randomly colliding sea ice floes shows an averaged viscous behavior in response to shearing sea ice motion, having strong resistance to compression and weak resistance to tensile stresses. This continuous rheology has its limitations. The VP formulation does not take into account the floe size distribution (Tilling et al. 2018; Horvat et al. 2019) in parameterizing the internal sea ice stress tensor. Also, the VP rheology is only suitable when floe sizes are much smaller than the computational grid size, typically for grid scales $>$ 20 km (Rothrock 1975). Hence, our idealized simulations of submesoscale dynamics in MIZs explicitly assume that the sea ice floes in lower sea ice concentration regimes are loosely packed (Toyota et al. 2006) and are sufficiently smaller than the grid size such that continuous assumption still holds. Thus, the VP parameterization of sea ice interactions may not behave accurately in high-resolution simulations when the size of some of the ice floes can exceed the grid size. Additionally, the continuous representation of sea ice limits the range of mixed layer eddy characteristics; for instance, eddies that might be generated at the floe boundaries of the leads would not be captured in a continuum model. Hence, the VP rheology can only explore the ice–ocean processes that are affected by statistical floe interactions and not by the interactions of a few individual floes or leads. At floe scales, the sea ice could be modeled as interacting Lagrangian particles using discrete element methods (e.g., Hopkins 2004; Herman 2016; Damsgaard et al. 2018; Turner et al. 2021).

The ocean component of the model solves hydrostatic, Boussinesq equations with an f-plane approximation. In this study, vertical mixing due to a variety of unresolved processes is parameterized with nonlocal K-profile parameterization (KPP) (Large et al. 1994), which sets vertical eddy diffusivity and viscosity. In our idealized experiments, submesoscale eddies evolve over short time scales (over a few days), and the eddy advection is dominant over surface thermodynamic forcing in that short time period. Thus, we argue that the thermodynamic forcing and associated sea ice growth/melt are important in generating horizontal density gradients and mixed layer fronts, but the frontal instabilities occur too fast to be directly affected by the buoyancy forcing. We thus turn the thermodynamic forcing off when considering the spindown of predefined fronts. This means that the sea ice is advected only by the ocean currents, and the mixed layer dynamics are purely driven by preexisting lateral buoyancy gradients.

The computational domain is a rectangular box, which has dimensions: L_x = 300 km, L_y = 200 km, and depth, H = 152 m while the computational grid size is [600 × 400 × 68]. To adequately resolve baroclinic instabilities in the mixed layer, the horizontal grid has a resolution of 500 m, while the vertical grid is stretched over 68 layers, varying from 0.2 m near the surface to 20 m near the bottom (maximum grid size in the mixed layer is 2 m). The computational domain is imposed with periodic boundary conditions in horizontal directions, with quadratic ice–ocean and bottom ocean stresses together with the no-buoyancy-flux boundary condition prescribed at the top and bottom boundaries.

b. Problem initialization

This study is focused on understanding the mixed layer eddy restratification under sea ice and assumes a spindown of a mixed layer front, similar with the setup used for the development of existing parameterization of mixed layer eddies (Fox-Kemper et al. 2008). As such, we do not address the reasons for the existence of the initial large-scale horizontal density gradients associated with surface fronts, acknowledging that those may have been formed after various events such as mesoscale frontogenesis, heterogeneous melting in MIZs, or wind-driven upwelling—processes omitted in our idealized study. Figure 1a illustrates fronts and dense filaments resulting in eddy-induced ageostrophic secondary circulation denoted by thick arrows and highlights downwelling and upwelling events at locations of cyclonic and anticyclonic filaments, respectively. The secondary circulation represents the restratification process via isopycnal slumping. The presence of sea ice can influence these surface convergence and divergence mechanisms at cyclonic and anticyclonic filaments, respectively. Sea ice internal stress acts to resist convergences at cyclonic filaments leading to a quasi-steady elevated sea ice mass distribution, while the divergences remain unarrested by sea ice rheology. This further leads to negative feedback and thus intensifies downwelling but diminishes upwelling (Manucharyan and Thompson 2017). To study these mechanisms, our model is initialized with a weakly vertically stratified mixed layer accommodating horizontal density gradients, and the interior has a uniform, strong vertical stratification as shown in Fig. 1. For simplicity of using double periodic boundary conditions, we prescribe two counterflowing jets with opposite horizontal density gradients at the surface, similarly to (Thomas 2008; Manucharyan and Timmermans 2013). Variations in the initial conditions of salinity in the cross-frontal Y direction are shown in Fig. 1c, and the top view of the surface ocean salinity is shown in Fig. 1d. Salinity profiles below the mixed layer match averaged ITP 77 hydrography [under-ice hydrographic properties from Ice-Tethered Profile 77 (Krishfield et al. 2008; Toole et al. 2011)], consistent with the MIZ simulations in Manucharyan and Thompson (2017). Crucially, the entire ocean surface is initially covered by sea ice with varying sea ice concentration, c, and a constant thickness, h = 2 m. In different numerical experiments, the initial sea ice concentration varies from 0% to 100% to cover a wide range of scenarios, from MIZs to packed or landfast ice.

For the numerical simulations, the analytical form of the initial density distribution is chosen as

$$\rho(y, z) = Z_S(z)\left[\Delta\rho_y Y_S(y) - \Delta\rho_z\right] + \rho_{\mathrm{ITP77}}(z), \tag{5}$$

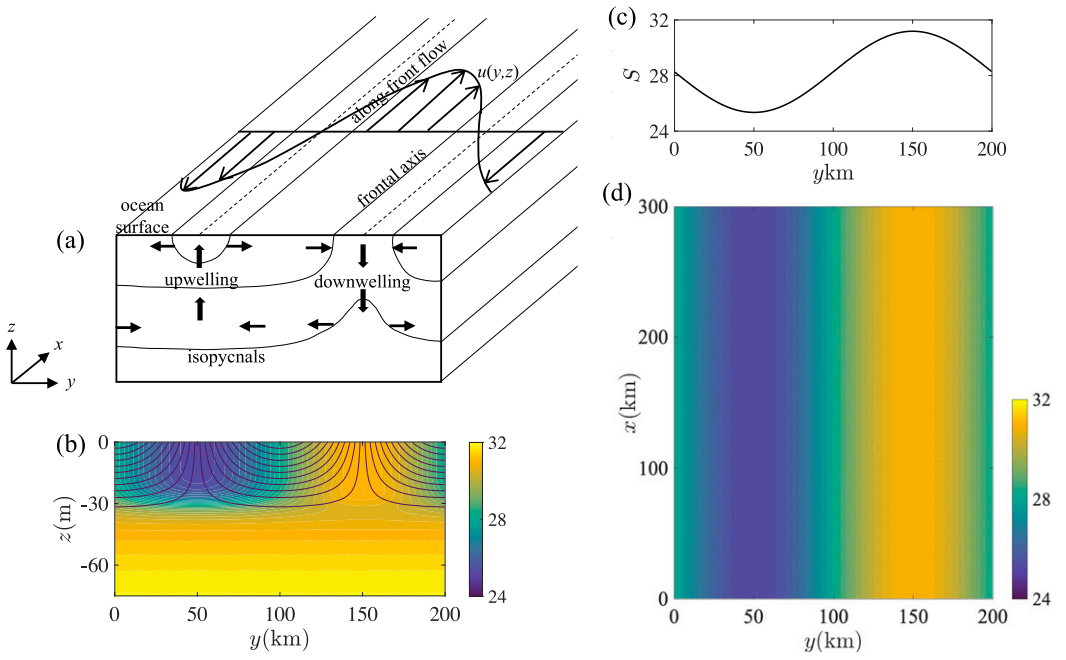

FIG. 1. Initial configuration for idealized MITgcm simulations to explore interactions of sea ice and submesoscale ocean variability in MIZ. (a) Sketch of ageostrophic secondary circulation formed as a result of mixed layer instabilities of large-scale flows with horizontal buoyancy gradients at the surface. The overturning circulation tends to slump the isopycnals and restratify the mixed layer. Also shown are the initial surface-intensified jets in the region between downwelling and upwelling zones. (b) Initial ocean stratification initialized with melt water fronts extending up to the mixed layer depth H_m that has bulk horizontal salinity difference ≈ 3, and with ITP 77 hydrography below the mixed layer. Black solid lines show contour lines of initial geostrophic velocity with 0.1 intervals. (c) Analytical form of the initial conditions of salinity that varies meridionally, and extends vertically until the mixed layer. (d) Top view of the ocean surface salinity contour that is analytically described in (c).

where

$$Z_S(z) = 0.5\left[1 + \tanh\left(\frac{-z + H_m}{\Delta h}\right)\right], \quad \text{and}$$

$$Y_S(y) = \sin\left(\frac{y - \frac{L_y}{2}}{2\pi L_y}\right).$$

In the above, $\Delta\rho_y$ is the bulk density difference across the front corresponding to the salinity difference $\Delta S \approx 3$, $H_m = 30$ m is the mixed layer depth, and parameters $\Delta\rho_z = \Delta\rho_y/2$ and $\Delta h = 5$ m. The f-plane approximation is used with the Coriolis parameter, $f = 1.4 \times 10^{-4}$ s^{-1}. A linear equation of state is used with a reference salinity $S_0 = 34$ psu, reference density $\rho_0 = 1027.5$ kg m^{-3}, and haline contraction coefficient $\beta = 1 \times 10^{-3}$ psu^{-1}. Since the thermodynamic sea ice growth/melt is turned off, the temperature of the ocean does not change, and the density is simply defined by the salinity. For the development of frontal instabilities, initial density distribution has been superimposed with small-amplitude white noise (Manucharyan and Timmermans 2013).

c. Methods

Fox-Kemper et al. (2008) showed that the restratification process could be cast in terms of an eddy-driven overturning streamfunction, following a similar parameterization idea proposed by Gent and McWilliams (1990) for mesoscale eddies. The ML restratification parameterization is as follows:

$$\Psi = \Psi_{c=0} = \frac{C_e H^2 \overline{\partial_y b}\,\mu(z)}{|f|}, \tag{6}$$

where $C_e = 0.06$–0.08, H is the mixed layer depth, $\overline{\partial_y b}$ is the horizontal buoyancy gradient, and $\mu(z)$ is the vertical structure of the overturning streamfunction. The overbar denotes horizontal and time averages. In our analysis, the streamfunction has been calculated in isopycnal coordinates, following the thickness-weighted averaging method (McIntosh and McDougall 1996; Abernathey et al. 2011):

$$\Psi(y,b) = \frac{1}{\Delta t L_x}\int_{t_0}^{t_0+\Delta t}\int_0^{L_x}\int_0^{b}(v'h')db^*\,dx\,dt.$$

Here, $h = -\partial z/\partial b$ is the layer thickness between isopycnals, and b^* is a dummy variable that represents isopycnal layers

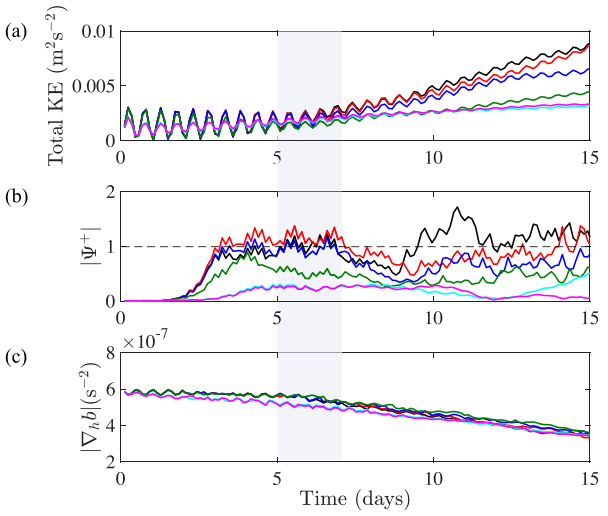

FIG. 2. Time evolution of (a) total kinetic energy, (b) nondimensional eddy-driven overturning streamfunction as defined in Eq. (7) that accounts for restratification process proceeding through baroclinic instabilities in the mixed layer and releasing mean potential energy, (c) horizontal buoyancy gradient where the potential energy is stored and the release of potential energy takes place once the mixed layer instabilities reach finite amplitude. Calculation of these quantities involve zonal averages + meridional averages within the domain region, y = 75–125 km, such that this study can be directly compared to the Fox-Kemper et al. (2008) parameterization where they consider only a single ML front. Black: c = 0 (Case C_{111}); red: c = 0.2 (Case C_{211}); blue: c = 0.5 (Case C_{311}); green: c = 0.65 (Case C_{411}); cyan: c = 0.8 (Case C_{511}); magenta: c = 1 (Case C_{611}).

for integration. [Figures 8a and 8b implement 21 discrete isopycnal layers using MITgcm Layers Package (Abernathey et al. 2011).] Moreover,

$$\overline{v'h'}^x = \overline{vh}^x - \overline{v}^x\overline{h}^x$$

is a meridional transport term, which defines the eddy streamfunction as a difference between the transport terms relating to residual mean streamfunction and the Eulerian mean streamfunction, respectively (McIntosh and McDougall 1996; Abernathey et al. 2011). Overbar with a superscript indicates averaging only along the specified coordinate. Thus, the averaging procedure considers zonal-mean and time-mean (averaged over 1 day, i.e., ~2 inertial periods, from day 5 to 6 in the shaded region in Fig. 2b) transport in isopycnal layers. Then, the streamfunction in the isopycnal coordinates is mapped into z coordinates by summing the layer thickness to calculate the depth of each layer (Andrews et al. 1987; McIntosh and McDougall 1996),

$$\Psi\left[y, \overline{b}^x(y,z)\right] = \Psi(y,b).$$

Then, it is meridionally averaged between y = 75 and 125 km in our study. The specified region covers a single ML front (Fig. 1), such that direct comparisons to the Fox-Kemper et al. (2008) parameterization can be made. Importantly, we have used a nondimensional form of the streamfunction in this study, which is defined as

$$\Psi^+ = \frac{\Psi}{\Psi_{c=0}} = \frac{\Psi}{C_e H^2 \overline{\partial_y b}\,\mu(z)/|f|}. \tag{7}$$

The main purpose here is to introduce a dimensionless parameter that easily measures a sea ice-induced change in the overturning streamfunction relative to the conventional ice-free parameterization. This yields $|\Psi^+| = 1$ for $c = 0$, and $|\Psi^+|$ reduces under the effect of sea ice ($c > 0$).

TABLE 1. List of numerical experiments used to assess the effect of sea ice cover on the eddy-driven streamfunction in the mixed layer. In the table, bold font indicates those simulations parameters that are varied while others are fixed.

Set	Case	c	C_d	ν_B (m^2 s^{-1})
1	C_{111}	**0**	5.35×10^{-3}	1×10^{-5}
	C_{211}	**0.2**	5.35×10^{-3}	1×10^{-5}
	C_{311}	**0.5**	5.35×10^{-3}	1×10^{-5}
	C_{411}	**0.65**	5.35×10^{-3}	1×10^{-5}
	C_{511}	**0.8**	5.35×10^{-3}	1×10^{-5}
	C_{611}	**1**	5.35×10^{-3}	1×10^{-5}
2	C_{521}	0.8	**0**	1×10^{-5}
	C_{531}	0.8	$\mathbf{0.67 \times 10^{-3}}$	1×10^{-5}
	C_{541}	0.8	$\mathbf{1.34 \times 10^{-3}}$	1×10^{-5}
	C_{551}	0.8	$\mathbf{2.67 \times 10^{-3}}$	1×10^{-5}
	C_{561}	0.8	$\mathbf{8.02 \times 10^{-3}}$	1×10^{-5}
	C_{571}	0.8	$\mathbf{10.7 \times 10^{-3}}$	1×10^{-5}
3	C_{621}	1	**0**	1×10^{-5}
	C_{631}	1	$\mathbf{0.67 \times 10^{-3}}$	1×10^{-5}
	C_{641}	1	$\mathbf{1.34 \times 10^{-3}}$	1×10^{-5}
	C_{651}	1	$\mathbf{2.67 \times 10^{-3}}$	1×10^{-5}
	C_{661}	1	$\mathbf{8.02 \times 10^{-3}}$	1×10^{-5}
	C_{671}	1	$\mathbf{10.7 \times 10^{-3}}$	1×10^{-5}
4	C_{512}	0.8	5.35×10^{-3}	$\mathbf{1 \times 10^{-4}}$
	C_{612}	1	5.35×10^{-3}	$\mathbf{5 \times 10^{-5}}$

d. Cases

The key parameters considered here are sea ice concentration (c), under-ice drag coefficient (C_d), and the background vertical viscosity and diffusivity (ν_B). Background vertical viscosity and diffusivity represent any unresolved turbulence-induced vertical mixing in the ocean interior that transfers momentum and energy upward against the buoyancy gradients. These parameters influencing the eddy dissipation are varied to reveal the system sensitivity to these parameters (Table 1) and establish a simple relationship between the overturning streamfunction and dissipation. All the other model parameters described above (section 2b) remain the same. This facilitates extending the Fox-Kemper et al. (2008) parameterization of ML restratification to idealized MIZ scenarios. The system sensitivity to the atmospheric wind forcing is out of the scope of this study and will be considered in future work.

In this regard, a series of simulation cases are uniquely identified by the given case nomenclature, C_{ijk}, where the indices i represent varying sea ice concentration, j represent

varying drag coefficient, and k represent varying background vertical viscosity. The parameter being varied is in bold. Also, we have grouped the simulations in different sets such that the influence of each parameter can be systematically tested. We have established that this range of idealized model simulations is sufficient to highlight the critical impact of sea ice on the eddy-driven mixed layer overturning.

3. Submesoscale eddies in the MIZ

Our simulations are initialized with a mixed layer front that is in a geostrophic balance. Over time, as the front spins down due to the development of ML instabilities and interactions with sea ice, it undergoes slumping of the near-vertical isopycnals by gravitational and eddy overturning, with the continuous Rossby adjustment process. Below we discuss the frontal and eddy evolution in ice-free and ice-covered conditions.

a. Ice-free eddy dynamics

The initial frontal adjustment lasts for around two days (Fig. 2), in which the total kinetic energy (Fig. 2a) and the lateral buoyancy gradient (Fig. 2c) oscillate with minor changes in amplitude. Similarly, the nondimensional eddy-driven overturning streamfunction, defined in Eq. (7), remains zero because the ML instabilities have not been developed yet (Fig. 2b). After ≈2 days, the restratification process starts to be dominated by the ML instabilities, at which point the extraction of potential energy (PE) stored in the lateral fronts occurs. The PE extraction is always positive and known to be maximum when the directions of buoyancy fluxes are along a surface that is one-half the angle of the mean isopycnal (Boccaletti et al. 2007). The PE release is reflected in the time evolution of the nondimensional eddy streamfunction $|\Psi^+|$ that increases in magnitude exponentially up to about day 3 (Fig. 2b). Once the eddies reach finite amplitude, the eddy fluxes start orienting parallel to the mean isopycnal surface, and the PE extraction rate decreases. This is when the vertical buoyancy fluxes reach a statistically steady state (Boccaletti et al. 2007). Between days 3 and 7, $|\Psi^+|$ remains statistically steady with magnitude of around 1, the total kinetic energy increases, and horizontal buoyancy gradients diminish.

When the eddy streamfunction is fully developed (days 3–7), the eddy length scales are about 3–7 km and $|\mathrm{Ro}| \approx 1$, indicating submesoscale dynamics. Following the linear stability analysis of Stone (1970), the eddy scales could be interpreted as the inverse growth rate τ_s and the wavelength L_s of the fastest-growing mode of the ML baroclinic instability:

$$\tau_s = \sqrt{\frac{54}{5}}\frac{\sqrt{1+\mathrm{Ri}}}{|f|},$$

$$L_s = \frac{2\pi U}{|f|}\sqrt{\frac{1+\mathrm{Ri}}{5/2}},$$

where Ri is the Richardson number and U is the mean shear velocity scale of the mixed layer front. For our experiments, $\mathrm{Ri} \approx 1$ implies that $\tau_s \approx 9.5$ h and $L_s \approx 6.5$ km, which are in agreement with the eddy scales at the early stages of the eddy development. However, after day 7, the submesoscale activity and the eddy streamfunction weaken as the eddies grow to over 10 km in size and their Rossby numbers drop substantially below 1, indicating mesoscale-like dynamics. The changes in the eddy characteristics likely result from an inverse energy cascade combined with the lack of formation of new submesoscale eddies due to the restratified mixed layer. In the subsequent quantitative analysis of eddy characteristics we use the time interval between days 5 and 7 (Fig. 2, shaded in gray), during which the submesoscale eddies are abundant and well developed.

b. Ice-covered eddy dynamics

The evolution of ML eddies changes dramatically when the full sea ice cover is present. Qualitative comparisons with the ice-free frontal instabilities imply that there is a time lag of ≈2 days in the development of baroclinic eddies and the variance of Ro is significantly lower at all times (Fig. 3). Quantitative comparisons of the surface ocean velocity magnitude, the integral eddy length scale, and the Rossby number variance demonstrate their strong dependence on the sea ice concentration (Fig. 4). The submesoscale eddies get weaker and smaller with increasing sea ice concentration, and these eddy characteristics exhibit a relatively sharp transition at a critical sea ice concentration of $c_{\mathrm{cr}} \approx 0.68$. Below this critical concentration, the presence of sea ice does not significantly affect the eddy dynamics and frontal spindown.

The basic effect of sea ice cover on the growth rate and wavelength of the most unstable wave can be understood by following the Eady–Ekman theory proposed by Williams and Robinson (1974). The Eady problem (Eady 1949) of baroclinic instability, in a simplified sense, can be interpreted as having two phase-locked boundary-trapped waves that mutually grow by extracting the potential energy from the mean flow. The Eady–Ekman problem is an extension to the Eady problem that adds the effect of boundary dissipation. Based on the theory, boundary dissipative effects introduced by the sea ice cover are concentrated in a thin top Ekman layer and can be represented by Ekman pumping, which modifies the upper boundary condition of the Eady problem. Displacement of fluid in the meridional direction favors the generation of positive buoyancy anomaly at the top and induces anticyclonic circulation. In the presence of the Ekman layer, the anticyclonic circulation drives Ekman pumping ($w < 0$) that favors negative buoyancy anomaly such that lighter fluid is advected downward. Ekman pumping strength is dependent on the friction imposed by the sea ice cover. Thus, Ekman pumping acts against horizontal disturbances and diminishes buoyancy perturbations at the top, which slows the top wave and alters its characteristics. This implies that the growth rate of baroclinic instability is reduced and selects a shorter wavelength (Brink and Cherian 2013; Chen et al. 2019).

The effect of sea ice cover on the submesoscale mixed layer restratification in a spindown problem is further explored using the insights from PV plots (Fig. 5). PV changes can be

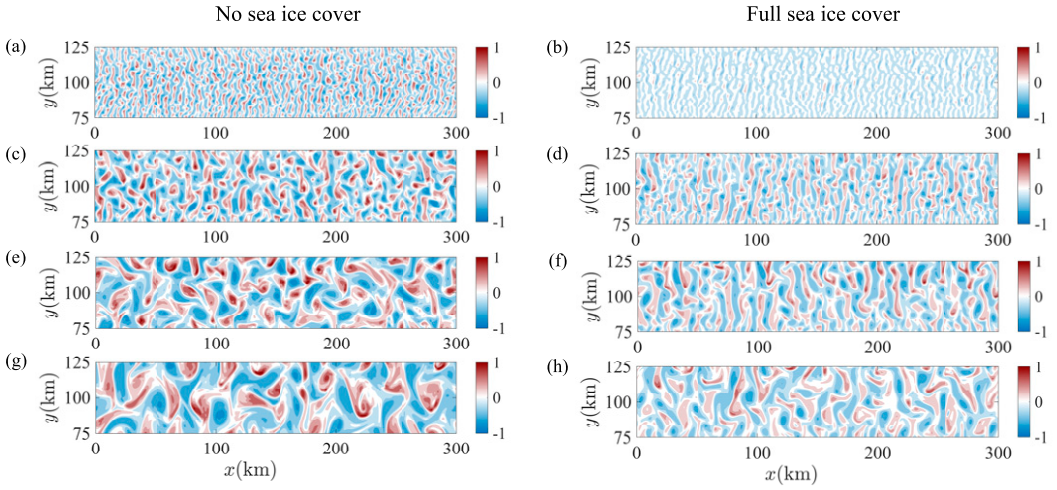

FIG. 3. Evolution of Rossby number (Ro = ζ/f, where ζ = vertical relative vorticity) at middepth of the mixed layer, z = 15 m for days ≈3, 6, 8, 11. (a),(c),(e),(g) Case C_{111} (c = 0) and (b),(d),(f),(h) Case C_{611} (c = 1).

associated with the restratification process (Haine and Marshall 1998), and therefore it is a highly useful tracer to study mixed layer dynamics of rotating stratified fluids. Various phenomena can result in PV changes and the associated restratification process in the upper ocean, such as frontogenesis, advection of PV, friction, and diabatic processes. The first two processes are conservative processes that only act to redistribute PV, while the last two are nonconservative processes associated with boundary layer turbulence and can modify PV. In our spindown experiments, friction is of leading-order importance. Since we assume that the fronts already exist in our simulations and disregard the frontogenesis process that might have resulted in the fronts, it can be excluded in the PV discussion. Also, our numerical experiments consider no surface heating/cooling, and thus PV modification due to the diabatic process is ruled out.

A spindown experiment with ice-free conditions (Figs. 5a,c) is imposed with no-stress top boundary condition, but the geostrophic shear is nonzero in the presence of a front at the surface. The mismatch between the no-stress top boundary condition and the geostrophic shear results in a frictional spindown of baroclinic current. It induces geostrophic Ekman buoyancy flux (Bachman and Taylor 2016) that acts to spindown the geostrophic current (Garrett and Loder 1981; Thompson 2000; Thomas and Rhines 2002; Thomas and Ferrari 2008). The Ekman transport is directed down the buoyancy gradient and thus, restratifies the fluid (Wenegrat and McPhaden 2016). In the PV perspective, surface boundary layer turbulence at submesoscale horizontal buoyancy gradients generate a source of PV at the ocean surface through turbulent thermal wind (TTW) balance. TTW flow develops an overturning circulation in the across-front direction that is downgradient at the surface, and thus, the PV flux is proportional to the restratification rate (Wenegrat et al. 2018). The frictional PV flux at the surface during spindown is given by, $\overline{J_z^F} = -(1/2)\sqrt{(2\nu/f)}|\nabla_h b|^2$. The overbar denotes horizontal and time averages. The frictional TTW PV flux is a negative definite quantity (Thomas and Ferrari 2008), which means the flux is directed downward regardless of the frontal orientation. The filaments of negative PV injecting into the ML can be seen in Fig. 5c. Further, the PV changes are observed throughout the ML in the spindown of geostrophic current due to the prevalent three-dimensional ML instabilities.

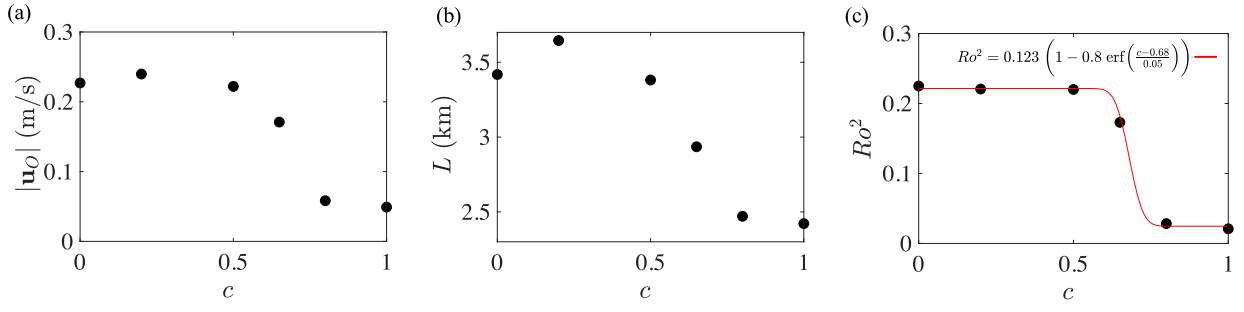

FIG. 4. Characteristics of ocean eddies for the frontal spindown experiments with varying sea ice concentrations. (a) Surface ocean velocity magnitude, (b) integral eddy length scale, and (c) variance of the Rossby number. A simple relationship is established between Ro^2 and c by fitting an error function. Calculations were performed for the center of the domain on day ≈6 when submesoscale eddies are well developed.

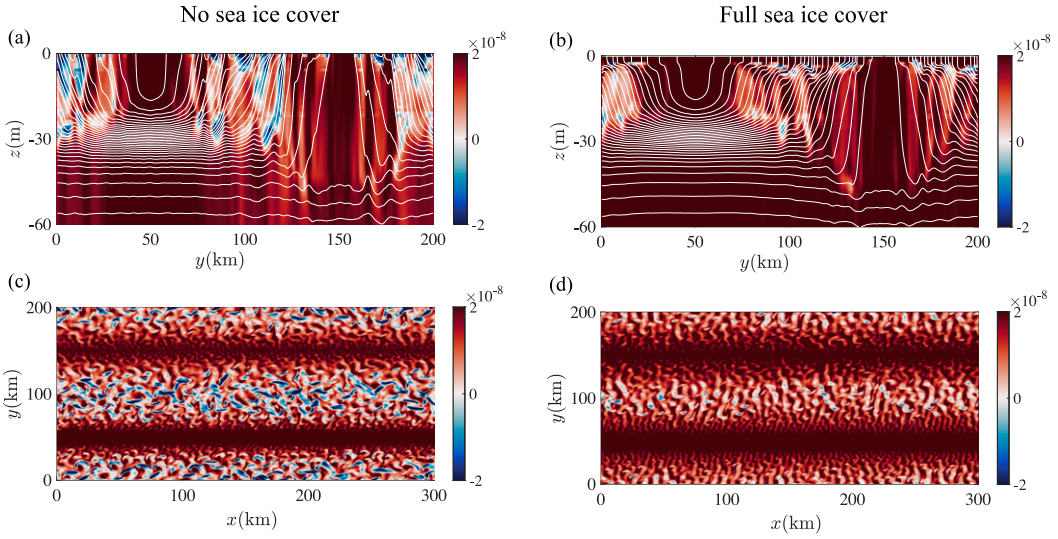

FIG. 5. Vertical section of potential vorticity (PV) at $y = 100$ km on day ≈6 of the spindown problem. White curves are isopycnals with 0.002 intervals. (a) $c = 0$; (b) $c = 1$. Also, horizontal sections of PV at mid of the mixed layer, $z = 15$ m on day ≈6 for (c) $c = 0$ and (d) $c = 1$. Unit of PV values shown in the color bar is s^{-3}. Areas of negative PV indicate conditions favorable for ageostrophic baroclinic instabilities. The figure highlights reduced submesoscale activity due to sea ice cover.

The lateral buoyancy gradient-driven ageostrophic secondary circulation, whose time scale is on the order of one day, quickly redistributes material properties within the mixed layer. This can be verified by Fig. 5, where the PV flux injects up to the base of the local mixed layer.

Under the effect of sea ice cover, the top boundary condition is close to no-slip, and therefore, the abovementioned mechanism to input vertical frictional PV flux is not valid anymore. However, the baroclinic current forced by the friction due to sea ice cover still injects downward flux of PV and restratifies the fluid in the mixed layer. Here, the Ekman flow that acts to spindown the geostrophic current is driven by the no-slip boundary condition induced wall shear stress instead of the "effective geostrophic stress" in the ice-free case. It can be seen in Figs. 5b and 5d that the PV flux at the surface due to sea ice cover friction is comparatively smaller, and the redistribution of PV by the eddy stirring is weaker (will be discussed more in upcoming sections) than ice-free conditions. It is also to be noted that the baroclinic instabilities are dampened by the sea ice cover that is reflected in lesser patches of negative PV (Figs. 5b,d).

Additionally, the evolution of sea ice over time for different mean sea ice concentration cases is shown in Fig. 6, and the associated videos are in the online supplemental material.

4. EKE budget analysis

The mixed layer EKE budget is analyzed in the frontal spindown experiments to examine the effect of the sea ice cover on the EKE production, advection, pressure work, tendency, and dissipation. The conversion rates from the mean to eddy kinetic energy (MKE to EKE) and eddy potential to eddy kinetic energy (EPE to EKE) can be estimated from the EKE budget analysis (Gula et al. 2016; Zhan et al. 2016; Renault et al. 2018). The EKE terms have been averaged horizontally and integrated vertically over the mixed layer, then time averaged over two inertial periods (~1 day) when the eddy streamfunction ($|\Psi^+|$) remained quasi steady. The EKE is calculated as $(1/2)\overline{u'^2}$, where primes denote deviations from the time mean for a quasi-steady flow. The EKE equation can be formed by subtracting the equation of the mean flow from that of the total flow and then multiplying the difference by velocity fluctuation vector (Pope 2000):

$$\frac{1}{2}\frac{\partial \overline{u_i'^2}}{\partial t} + \frac{1}{2}\frac{\partial \overline{u}_j \overline{u_i'^2}}{\partial x_j} = -\overline{u_i' u_j'}\frac{\partial \overline{u}_i}{\partial x_j} - \frac{1}{2}\frac{\partial \overline{u_i'^2 u_j'}}{\partial x_j} - \frac{1}{\rho_0}\frac{\partial \overline{u_j' p'}}{\partial x_j} + \overline{w'b'} - \epsilon, \tag{8}$$

where the overbar indicates temporal and horizontal averages, i are indices (1, 2), and j are indices (1, 2, 3). Also, $u_3 = w$ is the vertical velocity and $x_3 = z$ is the vertical coordinate.

The source of EKE in our frontal spindown problem is dominated by the conversion of EPE to EKE by fluxing buoyancy in the vertical, which is represented by $\overline{w'b'}$ (Fig. 7). The dominance of the $\overline{w'b'}$ term is the signature of the baroclinic instability as a mechanism of eddy generation. In an ice-free case, with no external forcing and zero-stress boundary conditions, there are no effective means of EKE dissipation and the baroclinic conversion acts only to increase EKE in the system. This implies a close balance between the EKE production

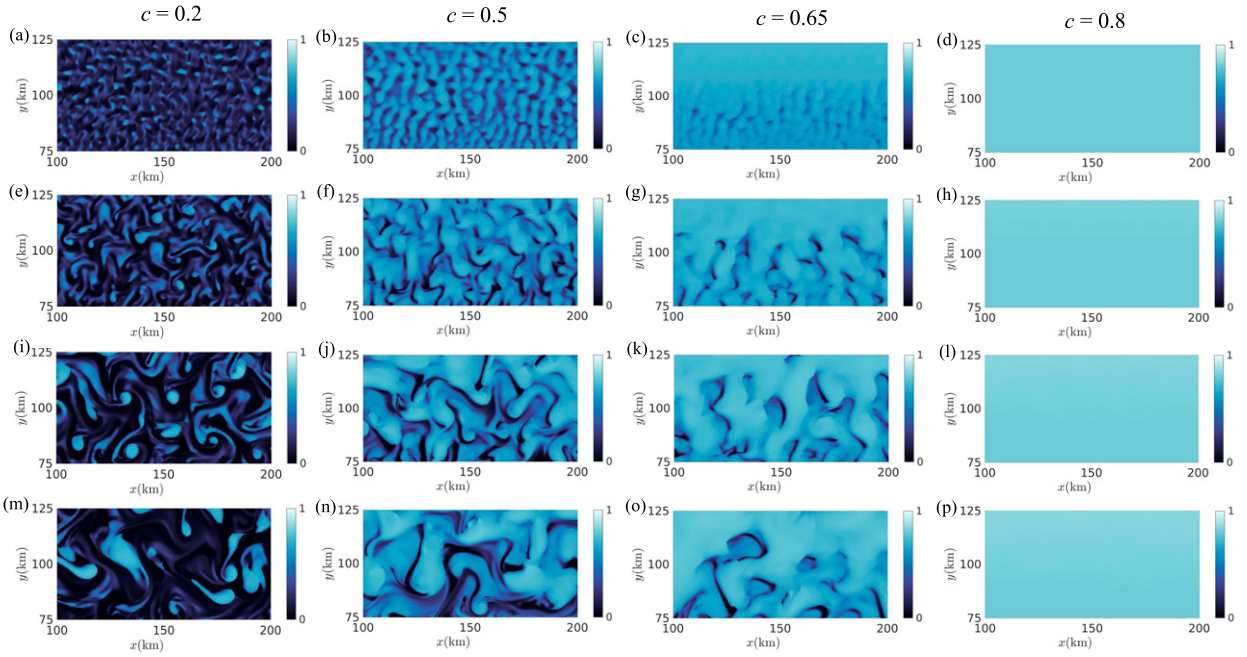

FIG. 6. Evolution of sea ice for days ≈3, 6, 8, 11. (a), (e), (i), (m) Case C_{211} (mean $c = 0.2$). (b), (f), (j), (n) Case C_{311} (mean $c = 0.5$). (c), (g), (k), (o) Case C_{411} (mean $c = 0.65$). (d), (h), (l), (p) Case C_{511} (mean $c = 0.8$).

and the EKE tendency term, $(1/2)\partial\overline{u_i'^2}/\partial t$, similarly to the frontal spindown simulations of Fox-Kemper et al. (2008).

The presence of a full sea ice cover ($c = 1$) introduces a substantial sink to the EKE budget that slows down the EKE accumulation (Fig. 7b). The sink is due to the sea ice–ocean drag and enhanced vertical mixing, represented by the last term in Eq. (8) as

$$-\epsilon = \frac{1}{\rho_0}\overline{\tau'_{i,I-O}u_i'}\Big|_{z=0} - (\nu_{\mathrm{KPP}} + \nu_B)\overline{u_i'\frac{\partial u_i'}{\partial z}}\Big|_{z=-H} - \int_{-H}^{0}\left[(\nu_{\mathrm{KPP}} + \nu_B)\overline{\left(\frac{\partial u_i'}{\partial z}\right)^2}\right]dz. \tag{9}$$

Thus, for a fully packed sea ice cover, the buoyancy production term and the dissipation term control the closure of the EKE balance, with a contribution from the EKE tendency rate. At intermediate sea ice concentrations, the buoyancy production decreases with increasing c value, and correspondingly the dissipation rate increases while the tendency rate decreases (see Fig. 2 in the online supplemental material). Contributions of the other transport terms: advection by the mean flow, $(1/2)\partial\overline{u_j}\overline{u_i'^2}/\partial x_j$; advection by turbulence, $(1/2)\partial\overline{u_i'^2u_j'}/\partial x_j$; and pressure transport, $(1/\rho_0)\partial\overline{u_j'p'}/\partial x_j$, are negligible for all sea ice concentration values, hinting at insignificant lateral or vertical eddy energy redistribution away from the mixed layer front. Thus, the EKE evolution in ice-covered fronts is determined by the buoyancy production due to mixed layer instabilities and the eddy dissipation induced by the ice–ocean drag and associated vertical mixing.

5. EKE dissipation and sea ice rheology

Here we develop scaling laws for the dependency of the EKE dissipation due to ice–ocean drag on sea ice concentration. For simplicity, we explore the limiting behaviors of the viscous-plastic sea ice rheology and consider a one-dimensional case. Neglecting Coriolis accelerations and atmospheric loading, and neglecting the sea surface height gradient term, the sea ice momentum conservation [Eq. (1)] can be written as follows:

$$\frac{1}{\rho}m\frac{\partial u_I}{\partial t} = cC_d u_*(u_O - u_I) + m\nu\nabla^2 u_I = 0, \tag{10}$$

where m is the sea ice mass per unit area that is defined as ch, and the Laplacian of the sea ice velocity represents the viscous regime of the viscous-plastic sea ice rheology (valid at lower sea ice concentrations, $c < c_{\mathrm{cr}}$). When the deformation parameter $\left\{\Delta = \left(\dot{\varepsilon}_d^2 + e^{-2}\dot{\varepsilon}_s^2\right)^{1/2}\right.$, where $\dot{\varepsilon}_d = \dot{\varepsilon}_{11} + \dot{\varepsilon}_{22}$ and $\left.\dot{\varepsilon}_s = \left[(\dot{\varepsilon}_{11} - \dot{\varepsilon}_{22})^2 + 4\dot{\varepsilon}_{12}^2\right]^{1/2}\right\}$ is less than a threshold, then sea ice can be treated as viscous fluid. To facilitate the analytical treatment, the ice–ocean stress parameterization is simplified to a linear drag law using u_* as the characteristic difference between ice and ocean velocity.

With the above simplifications, the steady-state sea ice x-momentum equation leads to the following balance:

$$cC_d u_*(u_I - u_O) = m\nu\nabla^2 u_I \sim m\nu\frac{u_I}{L^2}. \tag{11}$$

Here, $\nabla^2 u_I$ is scaled as u_I/L^2, where L represents the eddy length scale. Defining $C_d u_*/(\nu h) = B^2$, and after simple arrangements, we obtain the following scaling,

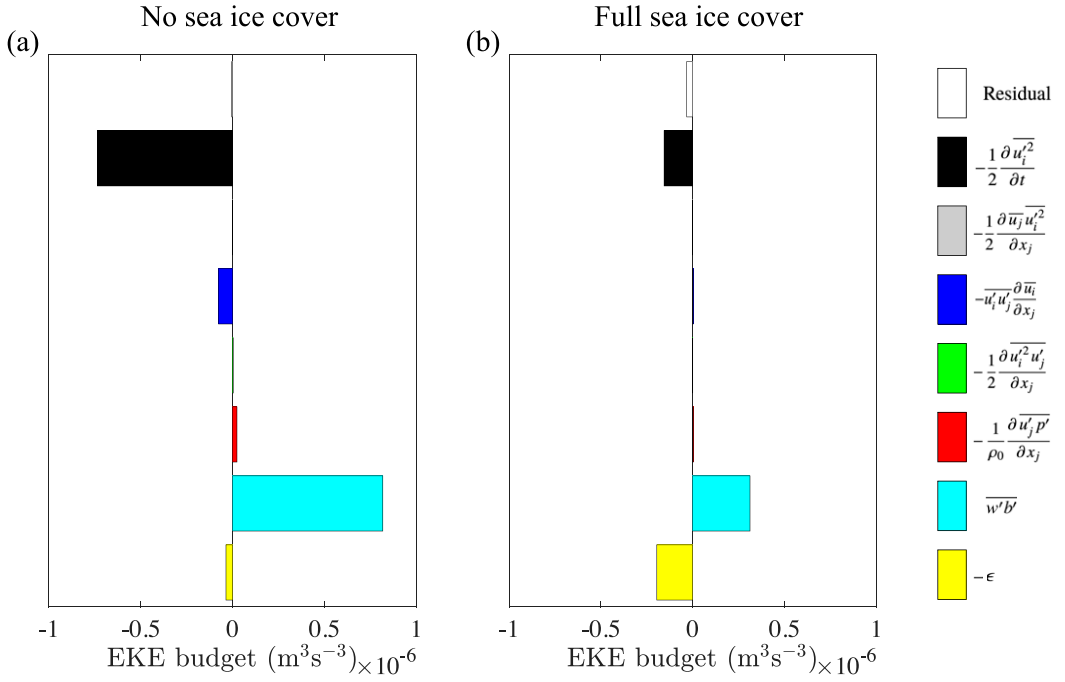

FIG. 7. Eddy kinetic energy budget: (a) $c = 0$ and (b) $c = 1$. EKE balance terms have been horizontally averaged then integrated in the vertical. Time averages are performed over two inertial periods within the shaded region in Fig. 2b. In ice-free scenario, EKE production rate is balanced by the tendency rate, while in the presence of sea ice cover the buoyancy production term and the dissipation term control the closure of the EKE balance, with a contribution from the EKE tendency rate.

$$\frac{u_I}{u_O} \sim \left(\frac{1}{1 - \frac{1}{B^2L^2}}\right). \tag{12}$$

Assuming $(BL)^{-2}$ is a small parameter, the right hand side can be further simplified by Taylor series expansion considering the terms up to the second order:

$$\frac{u_I}{u_O} \sim 1 + \frac{1}{B^2L^2}. \tag{13}$$

Further rearrangements yield a useful scaling law for the difference between the sea ice and surface ocean velocities:

$$u_I - u_O \sim u_O\left(\frac{1}{B^2L^2}\right). \tag{14}$$

The scaling law for the eddy dissipation due to an ice–ocean drag becomes

$$cC_d\,u_*(u_I - u_O)u_O \sim c\,C_d u_* u_O^2\left(\frac{1}{B^2L^2}\right).$$

Considering that it provides a major EKE sink (and/or that the mixing-induced dissipation scales similarly), the EKE dissipation scales as

$$|\epsilon| \sim cC_d\,u_*\,u_O^2\left(\frac{1}{B^2L^2}\right). \tag{15}$$

The parameter B contains sea ice viscosity that depends on the sea ice pressure and it, in turn, depends on the sea ice concentration, following the viscous-plastic rheology (Hibler 1979). Thus, $1/(B^2L^2)$ can be rewritten in the expanded form as

$$\frac{1}{B^2L^2} = \frac{\nu h}{C_d u_* L^2} = \frac{\frac{\mu}{\rho_I}h}{C_d u_* L^2} = \frac{\frac{P}{e_c^2\Delta}h}{\rho_I C_d u_* L^2} = \frac{h}{\rho_I C_d u_* L^2 e_c{}^2\Delta}\,P^* ch\left(e^{-C^*(1-c)}\right). \tag{16}$$

where $P = P^* che^{-C^*(1-c)}$ is a measure of sea ice strength, e_c is the ratio of major to minor axis in an elliptic yield curve that equals 2, and Δ is a bounding deformation parameter in the Hibler's sea ice rheology formulation. Here, the ratio of the semimajor and the semiminor axis, $e_c = 2$; sea ice thickness, h is an assumed constant; and P^* and C^* are constants that are generally set to 27 500 N m^{-2} and 20, respectively (Lemieux et al. 2010). For simplicity, Δ is considered constant and below the threshold such that the ice can be treated as a viscous fluid. Substituting Eq. (16) in Eq. (15), and taking $h^2P^*\Big/\left(\rho_I e_c^2\Delta\right) = J$, we obtain

$$|\epsilon| \sim J\,\frac{u_O^2}{L^2}\,c^2e^{-C^*(1-c)}. \tag{17}$$

Based on Fig. 4c, $\mathrm{Ro}^2 = 0.123\{1 - 0.8\mathrm{erf}[(c - 0.68)/0.05]\}$, and we know $u_O^2/L^2 \sim \mathrm{Ro}^2f^2$. Thus, Eq. (17) for the dissipation rate scaling becomes

$$|\epsilon| \sim K\left[1 - 0.8\,\mathrm{erf}\left(\frac{c - 0.68}{0.05}\right)\right]c^2 e^{-C^*(1-c)}. \tag{18}$$

However, the above scaling arguments are not appropriate when the sea ice concentration is higher than the critical sea ice concentration ($c_{cr} = 0.68$). In this regime, the linear-viscous assumption fails as the deformation parameter (Δ) exceeds the threshold value, and the sea ice behaves more like a plastic material. To elaborate on this, let us consider the limiting behavior for the fully packed sea ice with $c = 1$. This implies,

$$|\epsilon| \sim C_d u_* u_O^2. \tag{19}$$

Furthermore, since $u_I = 0$, u_O^2 equals ΔU^2. Additionally, it is known that $u_* \approx \sqrt{C_d}\Delta U$ (Lan-gleben 1982) and therefore, Eq. (19) can be rewritten as

$$|\epsilon| \sim u_*^3, \tag{20}$$

which agrees with the scaling arguments in Ou and Gordon (1986). The above scaling arguments are appropriate for all sea ice concentrations higher than the critical sea ice concentration ($c > c_{\mathrm{cr}}$) because, in this regime, sea ice apparently acts as a wall boundary and $u_I \approx 0$. Thus, the dissipation rate should scale as u_*^3 for $c > c_{\mathrm{cr}}$.

Bringing together Eqs. (18) and (20), we can define dissipation for a variety of MIZ conditions as

$$|\epsilon| \sim \begin{cases} K\left[1 - 0.8\,\mathrm{erf}\left(\frac{c - 0.68}{0.05}\right)\right]c^2 e^{-C^*(1-c)}, & \text{if } 0.68 \geq c \geq 0 \\ u_*^3, & \text{if } c > 0.68 \end{cases} \tag{21}$$

The scaling laws can be further transformed into a nondimensional form. In our simulations, the impact of thermodynamic forcing is neglected owing to the short time scales of the submesoscale flow under consideration. Also, we consider that the mean sea ice–ocean stress remains unaltered throughout the simulation. As such, u_*^3 should not change, allowing the nondimensional form of the dissipation rate for $c > c_{\mathrm{cr}}$ to be a constant (U^+). Thus,

$$|\epsilon^+| = \begin{cases} K^+\left[1 - 0.8\,\mathrm{erf}\left(\frac{c - 0.68}{0.05}\right)\right]c^2 e^{-C^*(1-c)}, & \text{if } 0.68 \geq c \geq 0 \\ U^+, & \text{if } c > 0.68 \end{cases}, \tag{22}$$

where the parameters K^+ and U^+ can be estimated by comparing Eq. (22) with the numerical results of the parametric study in Fig. 9. This gives, $K^+ = 430$ and $U^+ = 0.33$.

6. Ice-aware parameterization of the mixed layer overturning streamfunction

The strength of the eddy-driven streamfunction depends crucially on the presence of sea ice (Fig. 8). However, we will demonstrate below that its vertical structure and dependence on mixed layer depth and lateral buoyancy gradients remain similar to the ice-free parameterization [Eq. (6)]. This simplifies the parameterization of the overturning streamfunction to identify how its strength depends on sea ice concentration. We approach this problem by pointing out that the overturning strength is proportional to the buoyancy production term, and it, in turn, is correlated with the kinetic energy eddy dissipation due to ice–ocean drag.

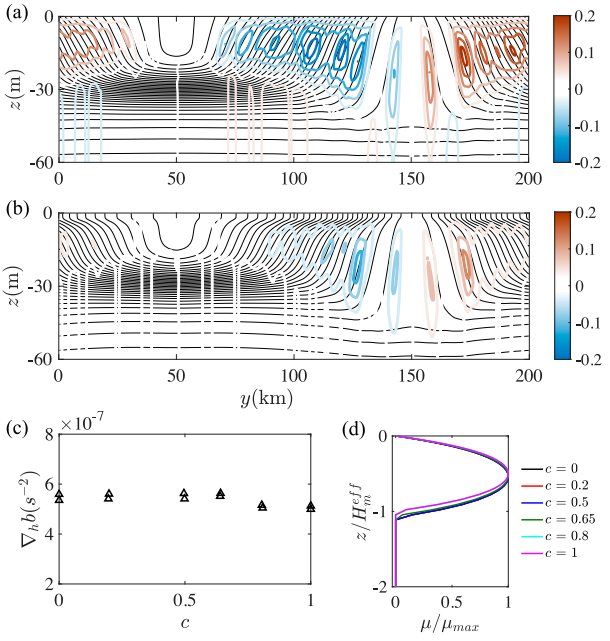

FIG. 8. Eddy-induced streamfunction contours mapped back to depth coordinates from isopycnal coordinates. The blue color represents clockwise rotation, while the red color represents counterclockwise rotation. Black contour lines denote mean isopycnals, and the contour interval is 0.002. (a) $c = 0$; (b) $c = 1$. (c) Comparison of horizontal buoyancy gradients for different values of sea ice concentration. Each of the symbols is the result of spatial averaging that involves zonal averages, meridional averages between $y = 75$ and 125 km, and time averaging over two different inertial periods within the shaded region in Fig. 2. One inertial period is between days 5 and 6, and another is between days 6 and 7. No significant changes in $\Delta_h b$ occur. (d) Comparison of normalized vertical structure of the overturning streamfunction, which is self-similar for all concentration values.

a. Overturning streamfunction under sea ice

Our numerical simulations were initialized with two fronts propagating in the opposite direction. As a consequence, there are cross-track deviations in all frontal and eddy field characteristics. The eddy overturning consists of two counter-rotating cells with a downwelling region on the saltier side and an upwelling on the fresher side (Fig. 8). The local mixed layer depth also varies in the cross-frontal direction, increasing from about 25 m in the upwelling region. For quantitative comparisons of the simulations with different sea ice covers, we consider the subdomain between $y = 75$ and 125 km. It lies

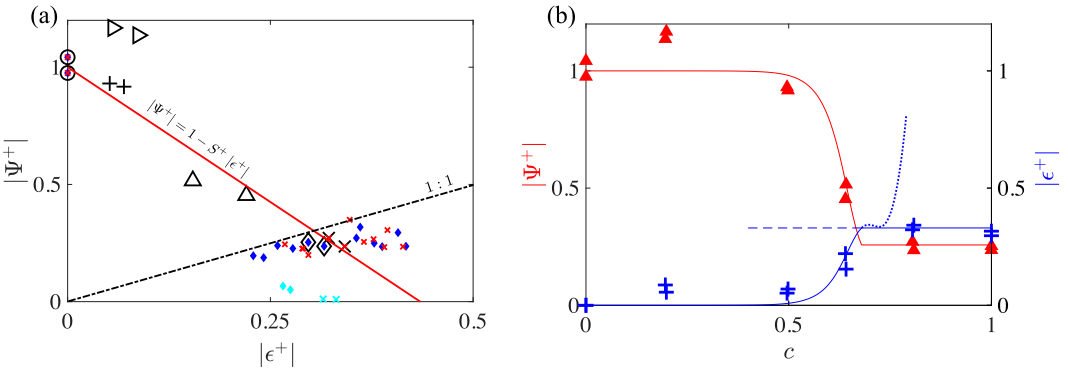

FIG. 9. (a) $|\Psi^+|$ vs $|\epsilon^+|$ for different spindown experiments. Black symbols indicate cases with varying c, while the parameters C_d and ν_B are fixed. Black circle, case C_{111}; black right-pointing triangle, case C_{211}; black plus, case C_{311}; black upward-pointing triangle, case C_{411}; black cross, case C_{511}; black diamond, case C_{611}. Red crosses indicate the cases with varying C_d for $c = 0.8$ and fixed $\nu_B = 1 \times 10^{-5}$ (Cases C_{521}, C_{531}, C_{541}, C_{551}, C_{561}, C_{571}. Blue solid diamonds indicate the cases with varying C_d for $c = 1$ and fixed $\nu_B = 1 \times 10^{-5}$ (Cases C_{621}, C_{631}, C_{641}, C_{651}, C_{661}, C_{671}). Cyan cross and cyan solid diamond denote cases C_{512} ($c = 0.8$) and C_{612} ($c = 1$) respectively, where ν_B varies while C_d is fixed. Dashed black line indicates 1:1 correspondence. Red solid line represents a linear regression line whose slope is 2.25. (b) $|\Psi^+|$ vs c is discussed with red solid triangles and red solid line, and $|\epsilon^+|$ vs c with blue pluses and blue solid line. The blue solid line represents Eq. (22) in section 5 that agrees well with the model simulation results (blue pluses). The blue dotted line and the dashed line show how Eq. (22) would behave beyond the prescribed sea ice concentration conditions. Furthermore, the red solid line represents Eq. (25) and depicts good fit to the model simulation results (red solid triangles).

between the upwelling and downwelling zones and covers a single ML front, such that direct comparisons to the Fox-Kemper et al. (2008) parameterization can be made. We note that the calculation of the streamfunction strength avoids a thin Ekman layer under the sea ice to make appropriate comparisons with the ice-free scenarios. The presence of the Ekman layer modifies the adiabatic nature of the eddy fluxes into diabatic near the surface of the ocean. But away from the surface boundary, the eddy fluxes are predominantly directed along isopycnals, with slight deviations due to the time dependency in a spindown problem. To remove inertial oscillations, we perform time averages over a period between days ~5 and 6, during which the submesoscale eddies have been developed, and the restratification process is at play.

The time-mean eddy overturning over the chosen subdomain is in a clockwise direction (negative streamfunction) and acts to slump the isopycnals with or without the sea ice cover (Figs. 8a,b). The strength of the streamfunction is significantly weaker under the full ice cover, reflecting the strong dampening of the ML eddies due to ice–ocean drag. However, sea ice does not significantly change the local mixed layer depth or the horizontal buoyancy gradients (Fig. 8). Likewise, the vertical structure of the eddy streamfunction normalized by the mixed layer depth H_m^{eff} remains the same for all sea ice concentrations (Fig. 8d). These observations imply that the nondimensional overturning streamfunction is dependent only on sea ice concentration, i.e., $|\Psi^+|$ is only a function of c.

b. Relation between the overturning strength and the dissipation rate

We define $|\epsilon^+|$ as the nondimensional dissipation term [similar to Eq. (22)] to represent the effect of sea ice–ocean drag:

$$\epsilon^+ = \frac{\overline{\tau_{i-o}\,u}/\overline{\partial_y b}}{\Psi_{c=0}}. \tag{23}$$

Sea ice induces damping of baroclinic instabilities and associated eddies, and hence the dissipation rate in the system is expected to depend on sea ice concentration. Similarly, $|\Psi^+|$ is a representative term for the production rate in the system and is a function of the sea ice concentration. As such, based on the dependency of both the terms on sea ice concentration, $|\Psi^+|$ is expected to be related to the dissipation rate. Indeed, we find an approximately linear relation between $|\Psi^+|$ and $|\epsilon^+|$ (Fig. 9a) under a range of conditions (see Table 1), including different sea ice concentrations (c), drag coefficients (C_d), and background viscosities (ν_B). As with the overturning strength, we defined the dissipation rate by spatially averaging in the alongfront direction in the cross-front direction between $y = 75$ and 125 km and depth-integrating within the mixed layer. The temporal averaging is performed for two different inertial periods: one between days 5 and 6, and another between days 6 and 7.

The parametric assessment shows that increasing sea ice concentration induces increased frictional drag that dissipates the mixed layer instabilities. This affects the isopycnal slumping process and thus undermines the submesoscale restratification. In other words, increasing sea ice concentration increases the dissipation rate that, in turn, reduces the strength of the overturning streamfunction. However, the parameter C_d has a minimal effect on the eddy-driven streamfunction. This is partially because the velocity difference between the sea ice and the upper ocean is inversely proportional to the ice–ocean drag coefficient (Manucharyan and Thompson 2017):

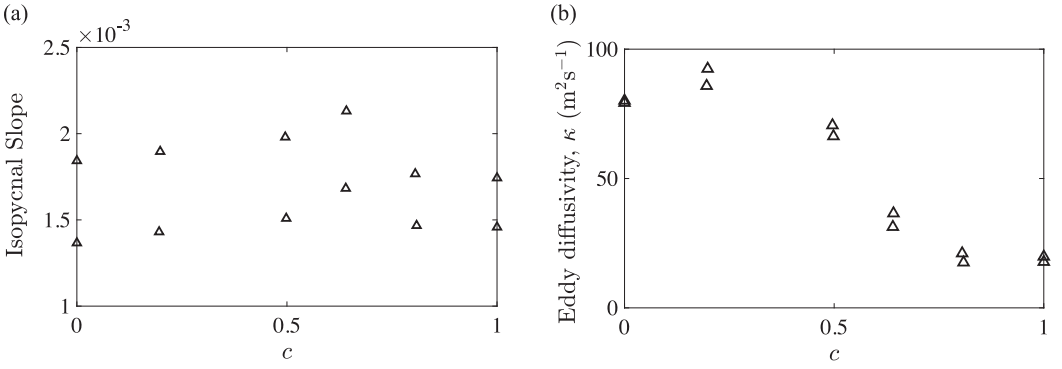

FIG. 10. (a) Isopycnal slope ($|\overline{\partial_y b}/\overline{\partial_z b}|$). (b) Eddy diffusivity $\left[\kappa = \left|\Psi/\left(\overline{\partial_y b}/\overline{\partial_z b}\right)\right|\right]$, as a function of sea ice concentration. Each of the symbols is the result of spatial averaging that involves zonal averages, meridional averages between $y = 75$ and 125 km, and time averaging over two different inertial periods within the shaded region in Fig. 2. One inertial period is between days 5 and 6, and another is between days 6 and 7. In Fig. 10b, κ vs c plot is largely dictated by the $|\Psi^+|$ vs c trend, and κ is on the order of $O(1–100)$ m^2 s^{-1} that drives reasonable restratification rates in the ML.

$$\frac{\Delta U}{u_0} \sim \frac{h}{R_d \mathrm{Ro} C_d}.$$

Note that increasing C_d to higher values shows a minimal effect, small values of C_d (close to 0) can effectively decouple the sea ice from the ocean. As such, cases with $c = 0$, $C_d = 5.35 \times 10^{-3}$ (Case C_{111}); $c = 1$, $C_d = 0$ (Case C_{621}); and $c = 0.8$, $C_d = 0$ (Case C_{521}) behave similarly as seen in the $|\Psi^+|$ versus $|\epsilon^+|$ plot (Fig. 9a). Further, varying the background viscosity ν_B mimics the effect of unresolved processes that could lead to enhanced vertical mixing, e.g., oscillating winds and breaking internal gravity waves. In our simulations, ν_{KPP} is dominant only in the surface layer (see Fig. 1 in the supplemental material), and ν_B takes over below it. An increase in ν_B drastically minimizes the overturning circulation. In conclusion, a linear regression provides a simple relation between $|\Psi^+|$ and $|\epsilon^+|$ expressed as

$$|\Psi^+| = 1 - S^+ |\epsilon^+|, \tag{24}$$

where slope (S^+) is estimated to be ≈2.25. The dashed black line in Fig. 9a indicates a 1:1 correspondence between the nondimensional streamfunction and dissipation rate. Points falling above or below this line indicate the excess of either the EKE production or dissipation, which is balanced by the EKE tendency rate (see section 4).

c. Parameterization of the overturning streamfunction

Using the linear relation between $|\epsilon^+|$ and $|\Psi^+|$ [Eq. (24)] and the dependency of $|\epsilon^+|$ on sea ice concentration formulated through scaling arguments [Eq. (22)], we write the parameterization for $|\Psi^+|$ as follows:

$$|\Psi^+| = \begin{cases} 1 - S^+ K^+ \left[1 - 0.8 \,\mathrm{erf}\left(\dfrac{c - 0.68}{0.05}\right)\right] c^2 e^{-C^*(1-c)}, & \text{if } 0.68 \geq c \geq 0 \\ C^+, & \text{if } c > 0.68 \end{cases}, \tag{25}$$

where the values of parameters S^+, K^+ have been estimated as 2.25 and 430, respectively. Based on scaling arguments in section 5, and Eqs. (22) and (24), for $c > c_{\mathrm{cr}}$, $|\Psi^+| \approx |\Psi^+|_{(c=1)} = C^+ = 1 - S^+ U^+ = 0.26$, where U^+ is estimated as 0.33. We know that the nondimensional streamfunction at zero sea ice concentration, $|\Psi^+|_{(c=0)} = 1$. Thus, R^+ can be defined as the ratio of $|\Psi^+|_{(c=0)}$ by $|\Psi^+|_{(c=1)}$, such that $R^+ = [|\Psi^+|_{(c=0)}/|\Psi^+|_{(c=1)}] = 1/C^+ = 3.8$ that indicates by how much the strength of overturning circulation has reduced due to the sea ice cover. The parameterization shows close agreement with the numerical simulations (Fig. 9b).

Similar to the parameterization by Gent and McWilliams (1990) for mesoscale eddy mixing, the restratification due to submesoscale eddies can also be expressed with a positive mean state eddy diffusivity κ, such that

$$\kappa = \frac{\Psi}{\overline{\partial_y b}/\overline{\partial_z b}} = \frac{\Psi^+ \Psi_{c=0}}{\overline{\partial_y b}/\overline{\partial_z b}}, \tag{26}$$

where Ψ^+ and $\overline{\partial_y b}/\overline{\partial_z b}$ are dependent on sea ice concentration (Fig. 10a). We find that κ versus c (Fig. 10b) is largely dictated by the $|\Psi^+|$ versus c trend, while the influence of $\overline{\partial_y b}/\overline{\partial_z b}$ on κ is relatively weak.

7. Sensitivity of the overturning parameterization to rheological parameters

The magnitudes of all stress tensor terms in the VP rheology are scaled to be proportional to the sea ice pressure, which is expressed in terms of the ice thickness and concentration [see Eq. (4) and Hibler (1979)]. There are two empirical constants in the formulation of the sea ice pressure, P^* and C^*, that are generally set to 27 500 N m^{-2} and 20 (Lemieux et al. 2010). The sea ice pressure scales with a strength parameter P^*, while its strong dependence on sea ice concentration (compactness) is expressed using C^*. These parameters propagated into our proposed parameterization of the overturning streamfunction for ice-covered fronts [Eq. (25)]. Thus, we explore the sensitivity of the

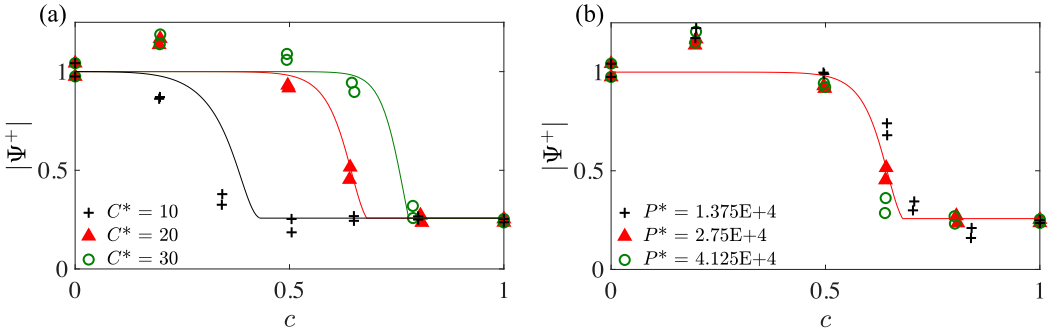

FIG. 11. The dependence of the nondimensional overturning streamfunction on the parameters (a) C^* and (b) P^* of the viscous-plastic sea ice rheology, plotted for frontal spindown experiments with different sea ice concentrations. Data points marked with same symbols represent experiments where a single rheological parameter was changed, with all other parameters fixed at their default values. The solid lines show the best fit using the ice-aware parameterization of the eddy streamfunction [Eq. (25)] after appropriately adjusting the C^* and c_{cr} values. Note, changes in P^* do not significantly affect the critical sea ice concentration so a single solid curve is plotted for all the data.

mixed layer overturning streamfunction to those two rheological parameters by conducting a set of additional numerical experiments.

The overturning streamfunction is highly sensitive to changes in C^* but less sensitive to P^* (Fig. 11). The reason for the high sensitivity to C^* is because this parameter appears inside an exponent in the dependence of sea ice pressure on the concentration, whereas P^* is only a prefactor [Eq. (4)]. As a consequence, decreasing C^* leads to a decrease in the critical sea ice concentration at which the transition to a weaker overturning occurs (Fig. 11a). The endpoints, $c = \{0, 1\}$, remain the same regardless of the rheological parameters because the rheology is irrelevant at zero concentrations, while for the fully packed sea ice, the explored rheological parameters lead to sufficiently strong sea ice that it does not substantially move under characteristic ice–ocean stresses. Thus, our proposed parameterization scheme [Eq. (25)] remains relevant for various rheological parameters, provided that the critical sea ice concentration is chosen accordingly (Fig. 11). While the exact functional form describing the streamfunction dependence on the sea ice concentration can be different for different rheological models, the transition between the two limiting cases (0% and 100% concentration) is expected to be nearly monotonic, with the transition occurring at a concentration for which the internal ice stresses reach the same order of magnitude as ice–ocean stresses associated with mixed layer eddies.

8. Summary and conclusions

We have investigated the influence of sea ice cover on submesoscale mixed layer dynamics in marginal ice zones using idealized numerical simulations of frontal spindown. The key result is that at sufficiently large sea ice concentrations, the ice–ocean drag dramatically suppresses the energetics of submesoscale mixed layer eddies and reduces the strength of the associated overturning streamfunction. Specifically, we found that the weakening of submesoscale eddies occurs abruptly at a critical concentration of about 0.7. This affects the isopycnal slumping process, leading to a reduction of the overturning streamfunction by a factor of 4 under the fully packed sea ice in comparison to ice-free conditions. Exploring the EKE budget, we established a simple linear relation between the EKE dissipation rate associated with the ice–ocean drag and the strength of the overturning streamfunction. Combining this relation with the derived scaling laws that explicitly link the dissipation rate to sea ice concentration (for viscous-plastic sea ice rheology), we proposed a parameterization of mixed layer restratification that explicitly depends on sea ice concentration [Eq. (25)].

Our ice-aware parameterization can be summarized as follows. The overturning streamfunction is

$$\Psi(c) = \Psi_{c=0}(1 - S^+|\epsilon^+|)$$

$$|\epsilon^+| = \begin{cases} K^+\left[1 - 0.8\,\mathrm{erf}\left(\dfrac{c - c_{cr}}{0.05}\right)\right]c^2 e^{-C^*(1-c)}, & \text{if } c \le c_{cr} \\ U^+, & \text{if } c > c_{cr}, \end{cases}$$

where $S^+ = 2.25$, $K^+ = 430$, $U^+ = 0.33, C^* = 20$, and $c_{cr} = 0.68$.

In the above expressions, $\Psi_{c=0}$ is the conventional parameterization of ML restratification (Fox-Kemper et al. 2008) that is already implemented in climate models. Our updated parameterization explicitly includes the dependency on sea ice concentration, predicting the sharp reduction of the overturning streamfunction as the sea ice concentration increases beyond the critical value of about 0.7. Since the transition between the two fixed limiting cases (0% and 100% concentration) is abrupt, the above equations can be approximated using a simple step function

$$\frac{\Psi}{\Psi_{c=0}} \approx \begin{cases} 1, & \text{if } c < c_{cr} \\ 0.26, & \text{if } c > c_{cr}. \end{cases}$$

The choice of the rheological model can affect the critical concentration and the sharpness of the transitional region,

but the endpoints (for $c = \{0, 1\}$) and the monotonic transition between them are expected to be robust. Thus, our proposed parameterization simply updates the existing MLE parameterization of Fox-Kemper et al. (2008) by including the dependency on sea ice concentration. Since current climate models do not use any ice-aware parameterizations of submesoscale eddies, the inclusion of the proposed parameterization in global climate models could improve the representation of sea ice–ocean interactions.

The strong reduction of submesoscale variability under sea ice is consistent with the observations of less energetic eddy dynamics under the packed ice (Timmermans et al. 2012) but appears at odds with some observational studies showing evidence of active MLIs in ice-covered regions (Gallaher 2019; Swart et al. 2020; Biddle and Swart 2020; Giddy et al. 2021). We thus emphasize that the simplified setup of our idealized numerical experiments neglects several factors that may affect the development of mixed layer instabilities, including the surface wind forcing, under-ice roughness conditions, and thermodynamic evolution of sea ice. Neglecting surface wind forcing eliminates the effect of wind–front interactions, and neglecting the thermodynamic evolution of sea ice avoids the increases in lateral buoyancy gradients associated with the brine rejection process during sea ice formation and lateral melt. Representing sea ice as a continuous media instead of a granular-like material neglects the impact of heterogeneous momentum and buoyancy fluxes associated with sea ice floes and leads. Assessing the influence of these additional processes on the frontal instabilities and associated overturning streamfunction is an important step in further improving the mixed layer parameterization.

Acknowledgments. This work was supported by the National Science Foundation (NSF), Division of Ocean Sciences, Award 1829969. The authors acknowledge the high-performance computing support from Cheyenne (doi:10.5065/D6RX99HX) provided by NCAR's CIS Laboratory, sponsored by the NSF. The authors thank Martin Losch for helping to debug a part of the MITgcm sea ice code essential to this study. The authors also acknowledge the helpful comments provided by an anonymous reviewer, Chris Horvat, and the editor.

Data availability statement. This article presents all information necessary to reproduce the numerical experiments. MITgcm configuration files can be found at https://doi.org/10.5281/zenodo.4435136.

REFERENCES

Abernathey, R. P., J. Marshall, and D. Ferreira, 2011: The dependence of southern ocean meridional overturning on wind stress. *J. Phys. Oceanogr.*, **41**, 2261–2278, https://doi.org/10.1175/JPO-D-11-023.1.

——, I. Cerovecki, P. R. Holland, E. Newsom, M. Mazloff, and L. D. Talley, 2016: Water-mass transformation by sea ice in the upper branch of the southern ocean overturning. *Nat. Geosci.*, **9**, 596–601, https://doi.org/10.1038/ngeo2749.

Andrews, D. G., J. R. Holton, and C. B. Leovy, 1987: *Middle Atmosphere Dynamics.* International Geophysical Series, Vol. 40, Academic Press, 489 pp.

Bachman, S. D., and J. R. Taylor, 2016: Numerical simulations of the equilibrium between eddy-induced restratification and vertical mixing. *J. Phys. Oceanogr.*, **46**, 919–935, https://doi.org/10.1175/JPO-D-15-0110.1.

——, ——, K. A. Adams, and P. J. Hosegood, 2017: Mesoscale and submesoscale effects on mixed layer depth in the Southern Ocean. *J. Phys. Oceanogr.*, **47**, 2173–2188, https://doi.org/10.1175/JPO-D-17-0034.1.

Biddle, L. C., and S. Swart, 2020: The observed seasonal cycle of submesoscale processes in the Antarctic marginal ice zone. *J. Geophys. Res. Oceans*, **125**, e2019JC015587, https://doi.org/10.1029/2019JC015587.

Boccaletti, G., R. Ferrari, and B. Fox-Kemper, 2007: Mixed layer instabilities and restratification. *J. Phys. Oceanogr.*, **37**, 2228–2250, https://doi.org/10.1175/JPO3101.1.

Brenner, S., L. Rainville, J. Thomson, and C. Lee, 2020: The evolution of a shallow front in the Arctic marginal ice zone. *Elem. Sci. Anth.*, **8**, 17, https://doi.org/10.1525/elementa.413.

Brink, K. H., and D. A. Cherian, 2013: Instability of an idealized tidal mixing front: Symmetric instabilities and frictional effects. *J. Mar. Res.*, **71**, 425–450, https://doi.org/10.1357/002224013812587582.

Buckley, J. R., T. Gammelsrod, J. A. Johannessen, O. M. Johannessen, and L. P. Roed, 1979: Upwelling: Oceanic structure at the edge of the Arctic ice pack in winter. *Science*, **203**, 165–167, https://doi.org/10.1126/science.203.4376.165.

Callies, J., R. Ferrari, J. Klymak, and J. Gula, 2015: Seasonality in submesoscale turbulence. *Nat. Commun.*, **6**, 6862, https://doi.org/10.1038/ncomms7862.

Chen, S.-H., C.-J. Chen, and J. A. Lerczak, 2019: On baroclinic instability over continental shelves: Testing the utility of Eady-type models. *J. Phys. Oceanogr.*, **50**, 3–33, https://doi.org/10.1175/JPO-D-19-0175.1.

Cohanim, K., K. X. Zhao, and A. L. Stewart, 2021: Dynamics of eddies generated by sea ice leads. *J. Phys. Oceanogr.*, **51**, 3071–3092, https://doi.org/10.1175/JPO-D-20-0169.1.

Csanady, G. T., 2001: *Air-Sea Interaction: Laws and Mechanisms.* Cambridge University Press, 248 pp.

Damsgaard, A., A. Adcroft, and O. Sergienko, 2018: Application of discrete element methods to approximate sea ice dynamics. *J. Adv. Model. Earth Syst.*, **10**, 2228–2244, https://doi.org/10.1029/2018MS001299.

Davy, R., and S. Outten, 2020: The Arctic surface climate in CMIP6: Status and developments since CMIP5. *J. Climate*, **33**, 8047–8068, https://doi.org/10.1175/JCLI-D-19-0990.1.

du Plessis, M., S. Swart, I. J. Ansorge, A. Mahadevan, and A. F. Thompson, 2019: Southern ocean seasonal restratification delayed by submesoscale wind–front interactions. *J. Phys. Oceanogr.*, **49**, 1035–1053, https://doi.org/10.1175/JPO-D-18-0136.1.

Eady, E. T., 1949: Long waves and cyclone waves. *Tellus*, **1**, 33–52, https://doi.org/10.3402/tellusa.v1i3.8507.

Ferrari, R., and C. Wunsch, 2009: Ocean circulation kinetic energy: Reservoirs, sources, and sinks. *Annu. Rev. Fluid Mech.*, **41**, 253–282, https://doi.org/10.1146/annurev.fluid.40.111406.102139.

Fox-Kemper, B., and R. Ferrari, 2008: Parameterization of mixed layer eddies. Part II: Prognosis and impact. *J. Phys. Oceanogr.*, **38**, 1166–1179, https://doi.org/10.1175/2007JPO3788.1.

——, ——, and R. Hallberg, 2008: Parameterization of mixed layer eddies. Part I: Theory and diagnosis. *J. Phys. Oceanogr.*, **38**, 1145–1165, https://doi.org/10.1175/2007JPO3792.1.

——, and Coauthors, 2011: Parameterization of mixed layer eddies. III: Implementation and impact in global ocean climate simulations. *Ocean Modell.*, **39**, 61–78, https://doi.org/10.1016/j.ocemod.2010.09.002.

Gallaher, S. G., 2019: The importance of capturing late melt season sea ice conditions for modeling the western Arctic Ocean boundary layer. *Elem. Sci. Anth.*, **7**, 53, https://doi.org/10.1525/elementa.391.

——, T. P. Stanton, W. J. Shaw, S. T. Cole, J. M. Toole, J. P. Wilkinson, T. Maksym, and B. Hwang, 2016: Evolution of a Canada basin ice ocean boundary layer and mixed layer across a developing thermodynamically forced marginal ice zone. *J. Geophys. Res. Oceans*, **121**, 6223–6250, https://doi.org/10.1002/2016JC011778.

Garrett, C. J. R., and J. W. Loder, 1981: Dynamical aspects of shallow sea fronts. *Philos. Trans. Roy. Soc.*, **A302**, 563–581, https://doi.org/10.1098/rsta.1981.0183.

Gent, P. R., and J. C. McWilliams, 1990: Isopycnal mixing in ocean circulation models. *J. Phys. Oceanogr.*, **20**, 150–155, https://doi.org/10.1175/1520-0485(1990)020<0150:IMIOCM>2.0.CO;2.

Giddy, I., S. Swart, M. du Plessis, A. F. Thompson, and S.-A. Nicholson, 2021: Stirring of sea-ice meltwater enhances submesoscale fronts in the Southern Ocean. *J. Geophys. Res. Oceans*, **126**, e2020JC016814, https://doi.org/10.1029/2020JC016814.

Gula, J., M. J. Molemaker, and J. C. McWilliams, 2016: Topographic generation of submesoscale centrifugal instability and energy dissipation. *Nat. Commun.*, **7**, 12811, https://doi.org/10.1038/ncomms12811.

Gupta, M., J. Marshall, H. Song, J.-M. Campin, and G. Meneghello, 2020: Sea-ice melt driven by ice-ocean stresses on the mesoscale. *J. Geophys. Res. Oceans*, **125**, e2020JC016404, https://doi.org/10.1029/2020JC016404.

Haine, T. W. N., and J. Marshall, 1998: Gravitational, symmetric, and baroclinic instability of the ocean mixed layer. *J. Phys. Oceanogr.*, **28**, 634–658, https://doi.org/10.1175/1520-0485(1998)028<0634:GSABIO>2.0.CO;2.

Herman, A., 2016: Discrete-element bonded-particle sea ice model design, version 1.3 a–Model description and implementation. *Geosci. Model Dev.*, **9**, 1219–1241, https://doi.org/10.5194/gmd-9-1219-2016.

Hibler, W. D. I., 1979: A dynamic thermodynamic sea ice model. *J. Phys. Oceanogr.*, **9**, 815–846, https://doi.org/10.1175/1520-0485(1979)009<0815:ADTSIM>2.0.CO;2.

Hopkins, M. A., 2004: A discrete element Lagrangian sea ice model. *Eng. Comput.*, **21**, 409–421, https://doi.org/10.1108/02644400410519857.

Horvat, C., and E. Tziperman, 2018: Understanding melting due to ocean eddy heat fluxes at the edge of sea-ice floes. *Geophys. Res. Lett.*, **45**, 9721–9730, https://doi.org/10.1029/2018GL079363.

——, and Coauthors, 2019: Estimating the sea ice floe size distribution using satellite altimetry: Theory, climatology, and model comparison. *Cryosphere*, **13**, 2869–2885, https://doi.org/10.5194/tc-13-2869-2019.

Klein, P., and G. Lapeyre, 2009: The oceanic vertical pump induced by mesoscale and submesoscale turbulence. *Annu. Rev. Mar. Sci.*, **1**, 351–375, https://doi.org/10.1146/annurev.marine.010908.163704.

Krishfield, R., A. Toole, A. Proshutinsky, and M.-L. Timmermans, 2008: Automated ice-tethered profilers for seawater observations under pack ice in all seasons. *J. Atmos. Oceanic Technol.*, **25**, 2091–2105, https://doi.org/10.1175/2008JTECHO587.1.

Langleben, M. P., 1982: Water drag coefficient of first-year sea ice. *J. Geophys. Res.*, **87**, 573–578, https://doi.org/10.1029/JC087iC01p00573.

Langmuir, I., 1938: Surface motion of water induced by wind. *Science*, **87**, 119–123, https://doi.org/10.1126/science.87.2250.119.

Large, W., J. McWilliams, and S. Doney, 1994: Oceanic vertical mixing: A review and a model with nonlocal boundary layer parameterization. *Rev. Geophys.*, **32**, 363–403, https://doi.org/10.1029/94RG01872.

Lemieux, J.-F., B. Tremblay, J. Sedlacek, P. Tupper, S. Thomas, D. Huard, and J.-P. Auclair, 2010: Improving the numerical convergence of viscous-plastic sea ice models with the Jacobian-free Newton-Krylov method. *J. Comput. Phys.*, **229**, 2840–2852, https://doi.org/10.1016/j.jcp.2009.12.011.

Losch, M., D. Menemenlis, P. Heimbach, J.-M. Campin, and C. Hill, 2010: On the formulation of sea-ice models. Part 1: Effects of different solver implementations and parameterizations. *Ocean Modell.*, **33**, 129–144, https://doi.org/10.1016/j.ocemod.2009.12.008.

Lu, K., T. Weingartner, S. Danielson, P. Winsor, E. Dobbins, K. Martini, and H. Statscewich, 2015: Lateral mixing across ice meltwater fronts of the Chukchi Sea shelf. *Geophys. Res. Lett.*, **42**, 6754–6761, https://doi.org/10.1002/2015GL064967.

Mahadevan, A., E. D'Asaro, C. Lee, and M. J. Perry, 2012: Eddy-driven stratification initiates North Atlantic spring phytoplankton blooms. *Science*, **337**, 54–58, https://doi.org/10.1126/science.1218740.

Manucharyan, G. E., and M. L. Timmermans, 2013: Generation and separation of mesoscale eddies from surface ocean fronts. *J. Phys. Oceanogr.*, **43**, 2545–2562, https://doi.org/10.1175/JPO-D-13-094.1.

——, and A. F. Thompson, 2017: Submesoscale sea ice-ocean interactions in marginal ice zones. *J. Geophys. Res. Oceans*, **122**, 9455–9475, https://doi.org/10.1002/2017JC012895.

Marshall, J., A. Adcroft, C. Hill, L. Perelman, and C. Heisey, 1997: A finite-volume, incompressible Navier Stokes model for studies of the ocean on parallel computers. *J. Geophys. Res.*, **102**, 5753–5766, https://doi.org/10.1029/96JC02775.

McIntosh, P. C., and T. J. McDougall, 1996: Isopycnal averaging and the residual mean circulation. *J. Phys. Oceanogr.*, **26**, 1655–1660, https://doi.org/10.1175/1520-0485(1996)026<1655:IAATRM>2.0.CO;2.

McWilliams, J. C., 2016: Submesoscale currents in the ocean. *Proc. Roy. Soc.*, **A472**, 1–32, https://doi.org/10.1098/rspa.2016.0117.

——, P. Sullivan, and C.-H. Moeng, 1997: Langmuir turbulence in the ocean. *J. Fluid Mech.*, **334**, 1–30, https://doi.org/10.1017/S0022112096004375.

Melville, W. K., 1996: The role of surface-wave breaking in air-sea interaction. *Annu. Rev. Fluid Mech.*, **28**, 279–321, https://doi.org/10.1146/annurev.fl.28.010196.001431.

Mensa, J. A., and M. L. Timmermans, 2017: Characterizing the seasonal cycle of upper-ocean flows under multi-year sea ice. *Ocean Modell.*, **113**, 115–130, https://doi.org/10.1016/j.ocemod.2017.03.009.

Molemaker, M., J. McWilliams, and M. K. Dewar, 2015: Submesoscale instability and generation of mesoscale anticyclones near a separation of the California Undercurrent. *J. Phys.*

Oceanogr., **45**, 613–629, https://doi.org/10.1175/JPO-D-13-0225.1.

Notz, D., and S. Community, 2020: Arctic sea ice in CMIP6. *Geophys. Res. Lett.*, **47**, e2019GL086749, https://doi.org/10.1029/2019GL086749.

Ou, H. W., 1984: Geostrophic adjustment: A mechanism for frontogenesis? *J. Phys. Oceanogr.*, **14**, 994–1000, https://doi.org/10.1175/1520-0485(1984)014<0994:GAAMFF>2.0.CO;2.

——, and A. L. Gordon, 1986: Spin-down of baroclinic eddies under sea ice. *J. Geophys. Res.*, **91**, 7623–7630, https://doi.org/10.1029/JC091iC06p07623.

Perovich, D. K., 2003: Thin and thinner: Sea ice mass balance measurements during SHEBA. *J. Geophys. Res.*, **108**, 8050, https://doi.org/10.1029/2001JC001079.

Pope, S., 2000: *Turbulent Flows.* Cambridge University Press, 802 pp.

Renault, L., J. C. McWilliams, and J. Gula, 2018: Dampening of submesoscale currents by air-sea stress coupling in the Californian upwelling system. *Sci. Rep.*, **8**, 13388, https://doi.org/10.1038/s41598-018-31602-3.

Roach, L. A., J. Dorr, C. R. Holmes, F. Massonnet, E. W. Blockley, D. Notz, and C. M. Bitz, 2020: Antarctic sea ice in CMIP6. *Geophys. Res. Lett.*, **47**, e2019GL086729, https://doi.org/10.1029/2019GL086729.

Rothrock, D. A., 1975: The mechanical behavior of pack ice. *Annu. Rev. Earth Planet. Sci.*, **3**, 317–342, https://doi.org/10.1146/annurev.ea.03.050175.001533.

Sallée, J.-B., R. J. Matear, S. R. Rintoul, and A. Lenton, 2012: Localized subduction of anthropogenic carbon dioxide in the southern hemisphere oceans. *Nat. Geosci.*, **5**, 579–584, https://doi.org/10.1038/ngeo1523.

Shrestha, K., W. Anderson, and J. Kuehl, 2018: Langmuir turbulence in coastal zones: Structure and length scales. *J. Phys. Oceanogr.*, **48**, 1089–1115, https://doi.org/10.1175/JPO-D-17-0067.1.

Smith, G. C., and Coauthors, 2019: Polar ocean observations: A critical gap in the observing system and its effect on environmental predictions from hours to a season. *Front. Mar. Sci.*, **6**, 429, https://doi.org/10.3389/fmars.2019.00429.

Spall, M. A., 1997: Baroclinic jets in confluent flow. *J. Phys. Oceanogr.*, **27**, 1054–1071, https://doi.org/10.1175/1520-0485(1997)027<1054:BJICF>2.0.CO;2.

Stone, P. H., 1970: On non-geostrophic baroclinic stability: Part II. *J. Atmos. Sci.*, **27**, 721–726, https://doi.org/10.1175/1520-0469(1970)027<0721:ONGBSP>2.0.CO;2.

Stroeve, J. C., M. C. Serreze, M. M. Holland, J. E. Kay, J. Malanik, and A. P. Barrett, 2012: The Arctic's rapidly shrinking sea ice cover: A research synthesis. *Climatic Change*, **110**, 1005–1027, https://doi.org/10.1007/s10584-011-0101-1.

Su, Z., J. Wang, P. Klein, A. F. Thompson, and D. Menemenlis, 2018: Ocean submesoscales as a key component of the global heat budget. *Nat. Commun.*, **9**, 775, https://doi.org/10.1038/s41467-018-02983-w.

Swart, S., M. D. du Plessis, A. F. Thompson, L. C. Biddle, I. Giddy, T. Linders, M. Mohrmann, and S.-A. Nicholson, 2020: Submesoscale fronts in the Antarctic marginal ice zone and their response to wind forcing. *Geophys. Res. Lett.*, **47**, e2019GL086649, https://doi.org/10.1029/2019GL086649.

Tandon, A., and C. Garrett, 1995: Geostrophic adjustment and restratification of a mixed layer with horizontal gradients above a stratified layer. *J. Phys. Oceanogr.*, **25**, 2229–2241, https://doi.org/10.1175/1520-0485(1995)025<2229:GAAROA>2.0.CO;2.

Thomas, L. N., 2008: Formation of intrathermocline eddies at ocean fronts by wind-driven destruction of potential vorticity. *Dyn. Atmos. Oceans*, **45**, 252–273, https://doi.org/10.1016/j.dynatmoce.2008.02.002.

——, and P. B. Rhines, 2002: Nonlinear stratified spin-up. *J. Fluid Mech.*, **473**, 211–244, https://doi.org/10.1017/S0022112002002367.

——, and C. M. Lee, 2005: Intensification of ocean fronts by down-front winds. *J. Phys. Oceanogr.*, **35**, 1086–1102, https://doi.org/10.1175/JPO2737.1.

——, and R. Ferrari, 2008: Friction, frontogenesis, and the stratification of the surface mixed layer. *J. Phys. Oceanogr.*, **38**, 2501–2518, https://doi.org/10.1175/2008JPO3797.1.

Thompson, A., A. Lazar, C. Buckingham, A. Naveira Garabato, G. Damerell, and K. Heywood, 2016: Open-ocean submesoscale motions: A full seasonal cycle of mixed layer instabilities from gliders. *J. Phys. Oceanogr.*, **46**, 1285–1307, https://doi.org/10.1175/JPO-D-15-0170.1.

Thompson, L., 2000: Ekman layers and two-dimensional frontogenesis in the upper ocean. *J. Geophys. Res.*, **105**, 6437–6451, https://doi.org/10.1029/1999JC900336.

Tietsche, S., and Coauthors, 2014: Seasonal to interannual Arctic sea ice predictability in current global climate models. *Geophys. Res. Lett.*, **41**, 1035–1043, https://doi.org/10.1002/2013GL058755.

Tilling, R. L., A. Ridout, and A. Shepherd, 2018: Estimating arctic sea ice thickness and volume using CryoSat-2 radar altimeter data. *Adv. Space Res.*, **62**, 1203–1225, https://doi.org/10.1016/j.asr.2017.10.051.

Timmermans, M. L., S. Cole, and J. Toole, 2012: Horizontal density structure and restratification of the Arctic Ocean surface layer. *J. Phys. Oceanogr.*, **42**, 659–668, https://doi.org/10.1175/JPO-D-11-0125.1.

Toole, J. M., R. A. Krishfield, M. L. Timmermans, and A. Proshutinsky, 2011: The ice-tethered profiler: Argo of the Arctic. *Oceanography*, **24**, 126–135, https://doi.org/10.5670/oceanog.2011.64.

Toyota, T., S. Takatsuji, and M. Nakayama, 2006: Characteristics of sea ice floe size distribution in the seasonal ice zone. *Geophys. Res. Lett.*, **33**, L02616, https://doi.org/10.1029/2005GL024556.

Turner, A. K., K. J. Peterson, and D. Bolintineanu, 2021: Geometric remapping of particle distributions in the discrete element model for sea ice (DEMSI v0.0). *Geosci. Model Dev. Discuss.*, https://doi.org/10.5194/gmd-2021-199.

Wenegrat, J. O., and M. J. McPhaden, 2016: Wind, waves, and fronts: Frictional effects in a generalized Ekman model. *J. Phys. Oceanogr.*, **46**, 371–394, https://doi.org/10.1175/JPO-D-15-0162.1.

——, L. N. Thomas, J. Gula, and J. C. McWilliams, 2018: Effects of the submesoscale on the potential vorticity budget of ocean mode waters. *J. Phys. Oceanogr.*, **48**, 2141–2165, https://doi.org/10.1175/JPO-D-17-0219.1.

Williams, G. P., and J. B. Robinson, 1974: Generalized Eady waves with Ekman pumping. *J. Atmos. Sci.*, **31**, 1768–1776, https://doi.org/10.1175/1520-0469(1974)031<1768:GEWWEP>2.0.CO;2.

Zhan, P., A. C. Subramanian, F. Yao, A. R. Kartadikaria, D. Guo, and I. Hoteit, 2016: The eddy kinetic energy budget in the Red Sea. *J. Geophys. Res. Oceans*, **121**, 4732, https://doi.org/10.1002/2015JC011589.

Zhang, J., and W. D. I. Hibler, 1997: On an efficient numerical method for modeling sea ice dynamics. *J. Geophys. Res.*, **102**, 8691–8702, https://doi.org/10.1029/96JC03744.